HELSINKI UNIVERSITY OF TECHNOLOGY
Faculty of Electronics, Communications and Automation

Maria Maksimow

TRANSIENT CURRENT TECHNIQUE (TCT) CHARACTERIZATION OF SILICON PARTICLE DETECTORS

Thesis submitted for examination for the degree of Master of Science in Technology

Espoo 26.3.2009

Thesis supervisor:

Prof. Harri Lipsanen

Thesis instructor:

D.Sc.(Tech.) Jaakko Härkönen

HELSINKI UNIVERSITY OF TECHNOLOGY

ABSTRACT OF THE MASTER'S THESIS

Author: Maria Maksimow

Title: Transient Current Technique (TCT) Characterization of Silicon Particle Detectors

Date: 26.3.2009 Language: English Number of pages: 8+53

Faculty: Faculty of Electronics, Communications and Automation

Professorship: Nanotechnology Code: S-104

Supervisor: Prof. Harri Lipsanen

Instructor: D.Sc.(Tech.) Jaakko Härkönen

In future high energy physics experiments, such as in the foreseen upgrade of the particle accelerator LHC at CERN, particle detectors will be exposed to significantly high particle radiation doses. Thus, extensive research is being conducted on improving the radiation hardness of silicon particle detectors and various defect and device engineering methods are examined. However, little data has been gathered especially from p-type magnetic Czochralski silicon (MCZ-Si) devices. This thesis presents the results of comparative transient current technique (TCT) measurements of both n-type and p-type MCZ silicon detectors as well as n-type Float Zone (FZ) silicon detectors. The results demonstrate that the MCZ silicon devices have superior radiation hard properties in comparison with the FZ silicon devices. Various examined parameters also suggest that p-type may be a more radiation hard material solution for silicon detectors than n-type MCZ silicon. Thus, replacing the currently installed FZ silicon detectors in LHC experiments with either n-type or p-type MCZ-Si devices is a viable option.

Keywords: TCT, silicon, radiation hardness, MCZ-Si, particle detector

TEKNILLINEN KORKEAKOULU

DIPLOMITYÖN TIIVISTELMÄ

Tekijä: Maria Maksimow

Työn nimi: Piihiukkasilmaisimien karakterisointi virtatransienttimenetelmällä

Päivämäärä: 26.3.2009 Kieli: Englanti Sivumäärä: 8+53

Tiedekunta: Elektroniikan, tietoliikenteen ja automaation tiedekunta

Professuuri: Nanotekniikka Koodi: S-104

Valvoja: Prof. Harri Lipsanen

Ohjaaja: TkT Jaakko Härkönen

Hiukkasilmaisimet altistuvat huomattavalle säteilylle tulevaisuudessa korkean energian hiukkasfysiikkakokeissa, esimerkiksi kun CERN:n hiukkaskiihdytin LHC ajanmukaistetaan. Näin ollen pii-ilmaisimien säteilynkestävyyden parantamista eli erilaisten säteilyn aiheuttamien kidevirheiden sekä ilmaisinsovellusten muokkaamista tutkitaan laajasti. Magneettisella Czochralski-menetelmällä (MCZ) valmistetuista kiekoista prosessoituja p-tyypin ilmaisimia on kuitenkin tarkasteltu melko vähän. Tässä työssä verrattiin sekä n- että p-tyypin MCZ-pii-ilmaisimia sekä float zone -menetelmällä (FZ) valmistetuista kiekoista prosessoituja n-tyypin ilmaisimia suorittamalla virtatransienttimittauksia (TCT). Tulokset osoittavat, että MCZ-piin sähköiset ominaisuudet ovat huomattavasti säteilynkestävämpiä kuin FZ-piin. Tutkittujen parametrien perusteella voidaan myös päätellä, että p-tyypin MCZ-pii saattaa olla säteilynkestävämpi ilmaisinmateriaali kuin n-tyypin MCZ-pii. Tämän työn tulokset tukevat siis oletusta, että LHC-kokeiden nykyisten FZ-pii-ilmaisimien vaihtaminen n- tai p-tyypin MCZ-ilmaisimiin olisi varteenotettava vaihtoehto.

Avainsanat: TCT, pii, säteilynkestävyys, MCZ-pii, hiukkasilmaisin

Preface

The work for this thesis was carried out in the CMS Tracker Project of the Helsinki Institute of Physics. The experimental research for the thesis was conducted at CERN in Geneva during summer 2008, and the thesis was written in autumn 2008 in the TKK Micronova facilities of the Helsinki University of Technology. The purpose of the work was to examine the radiation hardness properties of silicon particle detectors by Transient Current Technique measurements.

I would like to thank my supervisor Professor Harri Lipsanen for offering the possibility to work on this interesting subject. I am most indebted to my instructor Dr. Jaakko Härkönen for such focused guidance especially during the experimental part of the project. I am grateful for his patience in answering the same questions over and over again while, most importantly, showing a meaningful direction for the research project. I also wish to thank all the colleagues in the CMS Tracker Project both at CERN as well as in Otaniemi and Kumpula, who created a pleasant and often fun atmosphere I enjoyed working in.

I want to express heartfelt gratitude to my parents, Ursula and Paul, and my sister Christina, who have always supported me in all aspects of life. I would have never achieved anything without their love and trust. Finally, thank you, Robert, for lighting the Finnish winter darkness for me.

Otaniemi, 26.3.2009

Maria Maksimow

Contents

Symbols and Abbreviations

Symbols

A	active area of detector
C	capacitance
CCE	charge collection efficiency
CCE_g	geometrical factor of CCE
CCE_t	trapping induced factor of CCE
D	thickness of detector
D_n	diffusion constant of electrons
D_p	diffusion constant of holes
$E(x)$	electric field
E_{max}	maximum electric field
E_C	energy level of conduction band
E_F	Fermi energy level
E_g	band gap energy
E_t	activation energy
E_V	energy level of valence band
E_v	electric field caused by unit potential
$I(t)$	detector current
$i(t)$	transient current
I_{leak}	leakage current
J	current density
J_{gen}	generation current
J_n	electron current density
J_p	hole current density
J_s	saturation current
k_B	Bolzmann's constant
L_n	diffusion length of electrons
L_p	diffusion length of holes
n	density of electrons
N_{eff}	effective doping concentration
n_{eq}	1-MeV neutron equivalent
n_{p0}	density of electrons on the p-side in equilibrium
n_0	injected electron density
N_A	density of acceptor impurity atoms
N_C	density of states in the conduction band
N_D	density of donor impurity atoms
n_i	intrinsic carrier concentration
N_t	density of deep levels
N_V	density of states in the valence band
p	density of holes
p_{n0}	density of holes on the n-side in equilibrium
q	elementary charge
Q	collected charge
Q_0	total induced charge
Q_c	charge per unit area

T	absolute temperature
t	time
t_{dr}	drifting time
V	potential
V_{bi}	built in potential
v_{dr}	charge carrier velocity
V_{fd}	voltage of full depletion
v_t	thermal velocity
Vol	active volume of detector
W	width of depletion region
x_n	limit of depletion region on n-side
$-x_p$	limit of depletion region on p-side
α	current related damage rate
ϵ_s	permittivity of semiconductor
μ_n	mobility of electrons
μ_p	mobility of holes
Φ_{eq}	1-MeV neutron equivalent irradiation
ρ	electric charge density
σ	conductivity
$\sigma_{e,h}$	trapping cross section
τ_{detrap}	detrapping time constant
τ_{eff}	effective trapping time constant
τ_{gen}	generation lifetime

Abbreviations

ALICE	A Large Ion Collider Experiment
ATLAS	A Toroidal LHC Apparatus
CCE	charge collection efficiency
CERN	European Organization for Nuclear Research
CID	current injected detector
CMS	Compact Muon Solenoid
CSIC	Consejo Superior de Investigaciones Científicas
CZ	Czochralski
CZ-Si	Czochralski silicon
C–V	capacitance – voltage
DOFZ	diffusion oxygenated float zone silicon
e-h	electron – hole
FZ	Float Zone
FZ-Si	Float Zone Silicon
HEP	high energy physics
IMB-CNM	Instituto de Microelectrónica de Barcelona – Centro Nacional de Microelectrónica
I–V	current – voltage
LHC	Large Hadron Collider
LHCb	Large Hadron Collider beauty
MCZ	magnetic Czochralski
MCZ-Si	magnetic Czochralski silicon
MIP	minimum ionizing particle
NIEL	non-ionizing energy loss
poly-Si	polycrystalline silicon
PS	CERN Proton Synchrotron
RD39	CERN Collaboration: Cryogenic Tracking Detectors
RD48	CERN Collaboration: Research and development On Silicon for future Experiments (ROSE)
RD50	CERN Collaboration: Radiation hard semiconductor devices for very high luminosity colliders
SCR	space charge region
SCSI	space charge sign inversion
Si	silicon
SNR	signal to noise ratio
TCT	Transient Current Technique
TKK	Helsinki University of Technology

1 Introduction

The year 2008 has witnessed a milestone in experimental high energy physics (HEP) as the first beam circulated in the Large Hadron Collider (LHC) at the European Organization for Nuclear Research CERN after more than twenty years of planning and ten years of construction. The particle accelerator LHC, illustrated in Figure 1, and its four main experiments are the largest physics experiment in the world. The aim of the experiment is, among other things, to complete the Standard Model of particle physics, namely by finding experimental proof of the existence of the Higgs boson. [1]

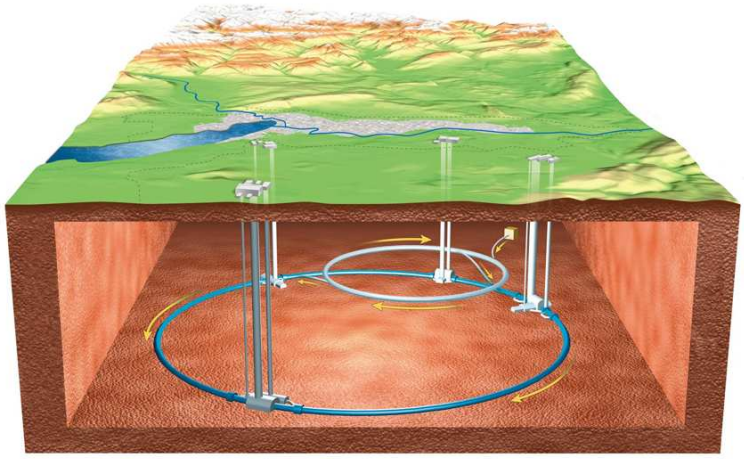

Figure 1: The Large Hadron Collider LHC is located 100 m underground close to Lake Geneva and the Jura mountains. [Image ©CERN]

The Higgs boson is believed to be a particle that transmits forces between matter particles. It is predicted by the Standard Model, which is currently the underlying theory of all particle physics. According to it, matter consists of two classes of elementary particles: quarks and leptons. Fundamental interaction forces act between these matter particles, the fermions, in form of energy exchange which is performed by carrier particles, the bosons. E.g., the electromagnetic force is one of these fundamental forces and the corresponding carrier particle is the photon.

The theory established by Peter Higgs and others suggests that both matter particles and carrier particles interact with a special force field via the Higgs boson. The

interaction with this Higgs field provides particles with mass relative to the amount of interaction. This would explain why some particles are heavier and others have nearly no mass at all.

However, the Higgs boson has not been experimentally detected, yet. Although no exact mass can be stated, it is predicted to be a rather heavy particle of more than 100 GeV/c^2 but possibly even over 500 GeV/c^2. Thus, the corresponding energy range has to be scanned thoroughly as the energy of the single particle in turn extends over a very small range. Moreover, a high repetition rate is needed, because the Higgs boson is very rare and the background noise has to be averaged out, as well. [2], [3]

Until now, experiments have not reached the required energies to observe the Higgs particle. This is the reason for the massive size of the LHC and its experiments, which also reach exquisite precision. The proton beams in the LHC consist of bunches of protons that are injected into the ring with a frequency of 40 MHz. This corresponds to collisions occuring within the detectors every 25 ns. The particle flux reaches $10^7 \frac{1}{s}$ in the closest region to the interaction vertex [4]. But even with this equipment, the production rate of the Higgs boson is expected to be rather moderate. Calculations propose that it takes at least 2–3 years before any reliable statistics have been collected from the data. [5]

The LHC itself is an accelerator ring built of 9300 magnets. It is located in a 27-km-long tunnel 100 m underground close to Geneva and the French-Swiss border. Protons or lead ions, which both belong to the group of hadrons, are accelerated around the ring in both directions in separate beam pipes. The magnets bend and focus the particle beam with such a high magnetic field that can only be achieved if the magnets are superconducting. Hence, the operating temperature of the accelerator magnets is only a few degrees from absolute zero. These procedures are necessary to control the particle beams precisely as the particles reach speeds close to light velocity and the energy of single protons rises up to 7 TeV. In fact, colliding the beams requires the same precision as shooting two needles from 10 km apart to

hit each other in the middle [6].

Collisions of the particles occur at the four main experimental sites of the LHC: ATLAS, CMS, ALICE, and LHCb. This work has been carried out in the framework of the Compact Muon Solenoid (CMS) experiment. The CMS is a general-purpose detector that is presented in Figure 2. While it is also designed for the search of the Higgs boson, the CMS is a suitable particle detector for any appearing particles with high energies reaching 2–3 TeV. Specific particles in this energy range and their decays could lead to progress in verifying theories such as supersymmetry and string theory. Research fields of dark matter, dark energy, and antimatter are desired to profit from the experiment, as well. [7]

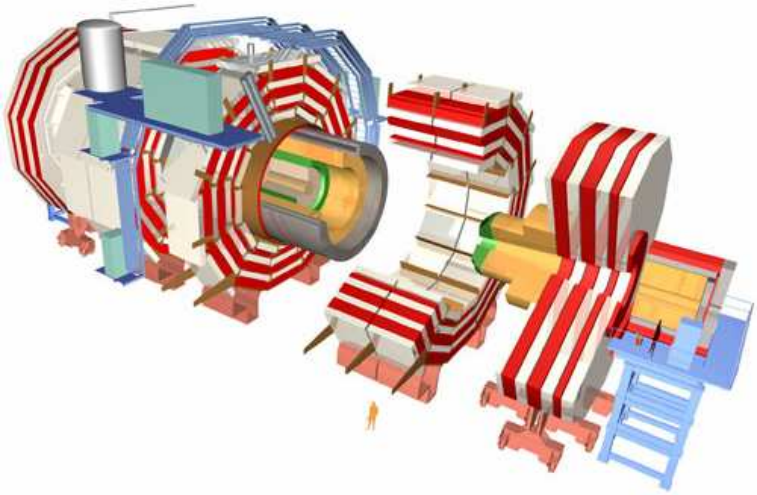

Figure 2: Schematic of the whole CMS Detector.[Image ©CERN]

A detector such as the CMS constitutes of a number of parts to identify different particles reliably. The main parts of CMS are the tracker for spatial locating of particle tracks, electromagnetic and hadronic calorimeters, and the muon system to track muons which permeate through the other detector parts undetected. [8] The all-silicon tracker system in CMS consists of different kinds of detectors [9]. Pixel detectors are located closest to the interaction point because the requirements for spatial resolution are the highest there. Behind the pixel detectors, silicon strip detectors are installed. When the products of the particle collisions spread radially from the collision point, obviously the silicon tracker is exposed to most extensive

particle radiation. The installation of the tracker system into the detector is shown in Figure 3.

The ability of silicon to withstand the deterioration of performance caused by radiation is called radiation hardness. However, the currently installed silicon pixel detectors in CMS are predicted to reach the limits of their functionality approximately within the next five years, whereas the strip detectors are predicted to stay functional for approximately ten years. This is the consequence of the excessive radiation luminosities described earlier.

The detectors currently in CMS were processed from silicon fabricated by the Float Zone (FZ) method. The purity of this type of silicon is considerably high and FZ-Si has therefore been favored as detector material. In the beginning of the 1990's the improving effect of oxygen on the radiation hardness of silicon was discovered [10]. After excessive research in the field of oxygenated silicon and its radiation hardness [11], the pixel detectors in CMS are indeed manufactured from Diffusion Oxygenated Float Zone (DOFZ) silicon. However, the disadvantage of the DOFZ method is the duration of the high temperature processing and therefore risk of contamination and cost.

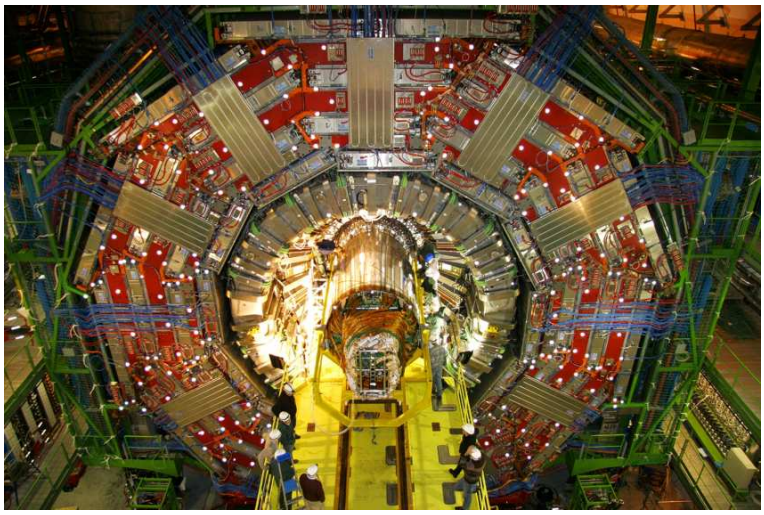

Figure 3: CMS Tracker installation.[Image ©CERN]

Approximately 10 years ago, development work in magnetic Czochralski (MCZ) crystal growth of high-resistivity silicon began. Electronics and semiconductor industry

had also evolved a demand for high-resistivity silicon, and commercial availability of high-resistivity MCZ-Si followed. Compared with FZ-Si, the oxygen concentration in MCZ-Si is evidently higher to begin with. Additionally, as the most used silicon type in industry, the growth of MCZ-Si is clearly less expensive than that of FZ-Si. Thus, the work to develop radiation hard particle detectors for the LHC upgrade from Czochralski silicon is of great interest.

A particularly well suited method for examining detectors is the Transient Current Technique (TCT) that has been developed by researchers of the Ioffe Institute in St. Petersburg, Russia and the Brookhaven National Laboratory in the USA [12]. It is a nondestructive testing method that enables studies of highly irradiated detectors more efficiently than, for example, traditional C–V measurements. TCT allows to determine various parameters, such as the voltage of full depletion, to characterize the detectors. Until now, little research has generally been conducted on p-type MCZ-Si detectors. This thesis project focuses on comparative TCT measurements of MCZ-Si detectors fabricated of both n- and p-type silicon bulk. Detectors of FZ-Si are included in the studies as well for comparison.

This thesis presents in Chapters 2 and 3 the theoretical background for silicon particle detectors and their radiation hardness. Chapter 4 concentrates on the method of TCT describing both the principle of the technique as well as the performed practical measurements. The results are presented and discussed in Chapter 5, and Chapter 6 summarizes the contents.

2 Silicon Detectors

Silicon particle detectors used in the LHC experiments are in principle reverse biased p-n diodes. The highly doped implantations are formed on both sides of the silicon wafer to create volume devices. When the bias voltage is applied, the electric field extends over the whole detector thickness. The energy of incoming particles generates pairs of free charge carriers in the bulk that drift to opposite sides of the detector and are collected there. Although Brattain and Bardeen developed the point-contact transistor in the early 1950's, it was W. Shockley who established the theory of the p-n junction and suggested its practical use in electronic devices. The theory presented in Section 2.1 is based on [13].

2.1 p-n Junction

In practice, a p-n junction is usually fabricated by diffusion or implantation of acceptor- or donor-type impurity atoms into n- or p-type substrate silicon, respectively. In theory, however, a p-n junction is usually described as an abrupt junction combined of two originally independent parts; one part being p-type, the other n-type. The term abrupt junction describes a state in which the impurity atom concentration changes abruptly over the junction interface from acceptors to donor atoms as depicted in Figures 4a) and 4b). Furthermore, a one-sided junction results when the impurity density is significantly higher on one side of the junction than on the other side.

When the p-type and n-type regions form a common interface, the free carriers of both sides diffuse to the other side of the junction and recombine. Electrons move in direction of the p-region and leave positive donor ions behind until x_n. Negatively charged acceptor ions occupy the p-type region until $-x_p$ as holes diffuse to the n-side. The region containing the ionized impurity atoms is empty of free charge carriers and is thus called the depletion region or space charge region (SCR). The limits $-x_p$ and x_n of the depletion region are shown in Figure 4. Thermal equilibrium is reached when there is no net current flow.

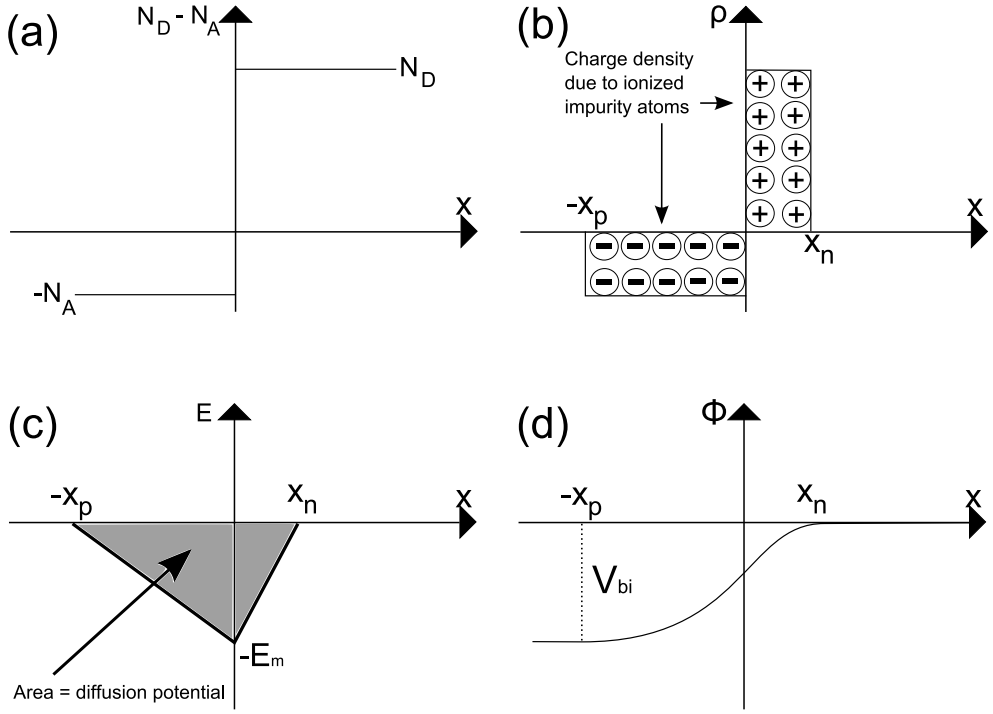

Figure 4: Properties of an abrupt p-n junction: a) density of impurity atoms; b) space charge density; c) distribution of the electric field; and d) potential distribution over the junction.

The Fermi energy level E_F in p-type semiconductors is close to the valence band E_v and close to the conduction band E_c in n-type semiconductors. As a result, the conduction and valence bands are bent in the junction region because the Fermi level has to stay constant over the junction to satisfy the condition of zero current flow. The bending of the energy bands leads to a built-in potential V_{bi}; i.e., qV_{bi} is the difference in energy between the original E_F levels in the n- and p-regions. For silicon p-n junctions, V_{bi} has a value of approximately 0.7 V. V_{bi} can as well be understood as the corresponding potential to the electric field which is generated in the depletion region between the space charges opposite in charge. The distribution of potential over the junction is presented in Figure 4d).

The p-n junction can be described mathematically starting from Poisson's equation in one dimension:

$$\frac{dE}{dx} = \frac{\rho}{\epsilon_s}. \tag{1}$$

E is the electric field across the junction and ϵ_s the permittivity of the semiconduc-

tor. The electric charge density ρ can be approximated with the product of unit charge and the corresponding doping atom concentration: $-qN_A$ for acceptors and qN_D for donors if all impurities are assumed to be ionized. The electric field being the negative first derivative of the potential, we get:

$$-\frac{d^2V}{dx^2} = \frac{qN_D}{\epsilon_s} \quad \text{for} \quad 0 < x \leq x_n \tag{2}$$

$$\text{and} \qquad \frac{d^2V}{dx^2} = \frac{qN_A}{\epsilon_s} \quad \text{for} \quad -x_p \leq x < 0. \tag{3}$$

As can be seen in Figure 4c), the electric field across the junction is zero at $-x_p$ and x_n. The maximum of the field, E_{max}, is located at $x = 0$. Thus, Equation 1 can be integrated over x to obtain for the p-side:

$$E(x) = -\frac{qN_A}{\epsilon_s}(x + x_p). \tag{4}$$

The calculation for the n-region is analog. The following is valid for the maximum of the electric field at the junction contact:

$$|E_{max}(x = 0)| = \frac{qN_A x_p}{\epsilon_s} = \frac{qN_D x_n}{\epsilon_s}. \tag{5}$$

Integrating Equations 2 and 3 twice and adding the results, we get the total diffusion potential:

$$\begin{aligned} V_{bi} &= \frac{1}{2}\frac{qN_A}{\epsilon_s}x_p^2 - \frac{1}{2}\frac{qN_D}{\epsilon_s}x_n^2 \\ &= -\frac{1}{2}E_{max}(x_p + x_n) = -\frac{1}{2}E_{max}W \end{aligned} \tag{6}$$

Equation 6 introduces the depletion width W that denotes the width of the space charge region from $-x_p$ to x_n. When x_n and x_p are solved from Equation 5 in dependence of E_{max}, their sum becomes

$$x_n + x_p = E_{max}\frac{\epsilon_s}{q}\left(\frac{1}{N_A} + \frac{1}{N_D}\right). \tag{7}$$

E_{max} is solved from Equation 6 and inserted in Equation 7, so W results in:

$$W = \sqrt{\frac{2\epsilon_s V_{bi}}{q}\left(\frac{N_A + N_D}{N_A N_D}\right)}. \tag{8}$$

If the junction is one-sided with $N_D >> N_A$, and it is assumed that neither the depletion region extends over the limits of W nor are any charge carriers left in the SCR, then Equations 5 and 6 yield:

$$W = \sqrt{\frac{2\epsilon_s V_{bi}}{qN_A}}. \tag{9}$$

Again, the calculation is analog, if $N_A >> N_D$. The depletion width extends to the side of the junction with lighter doping concentration, because the condition of total charge neutrality has to be fulfilled. As a consequence, it is possible and desirable to increase the depletion width through the whole detector thickness D by biasing the detector with sufficient reverse voltage, namely the full depletion voltage V_{fd}. Thus, when $D = W$, Equation 9 transforms to

$$V_{bi} - V_{fd} = \frac{qN_A D^2}{2\epsilon_s} \tag{10}$$

for a one-sided p-type detector. According to Equation 10, the options to achieve a depletion voltage as low as possible include reducing the doping concentration of the bulk and using thin detectors. The effective doping concentration is often denoted with N_{eff}, when

$$N_{eff} = N_D - N_A. \tag{11}$$

Applied voltage V changes the charge per unit area, Q_c, in the active detector volume. This is the definition for the depletion-layer capacitance per unit area:

$$C \equiv \frac{dQ_c}{dV}. \tag{12}$$

Using Equation 9, C for a one-sided abrupt junction can be written as:

$$C = \frac{\epsilon_s}{W} = \sqrt{\frac{q\epsilon_s N_A}{2(V_{bi} - V)}}, \quad W \leq D,\, V \leq V_{fd} \tag{13}$$

When the external voltage reaches V_{fd}, the detector is fully depleted. As a result, the overall capacitance saturates to a value solely dependent on geometrical factors:

$$C = \frac{\epsilon_s A}{D}. \tag{14}$$

A is the active area of the diode. Consequently, the voltage of full depletion can be determined, e.g., by C-V measurements, from the saturation point of the capacitance.

The ideal diode law for current-voltage characteristics is the Shockley equation:

$$J_s = \frac{qD_p p_{n0}}{L_p} + \frac{qD_n n_{p0}}{L_n}, \tag{15}$$

where J_s is the saturated diffusion current when no electric field is present. D_p (D_n) is the diffusion constant of holes (electrons), p_{n0} (n_{p0}) is the equilibrium hole (electron) density on the n-side (p-side), and L_p (L_n) denotes the diffusion length of holes (electrons).

In a reverse-biased detector, current is generated in the depleted layer, which is exposed to an electric field. The generation current J_{gen} can be expressed as:

$$J_{gen} = \frac{qn_i W}{\tau_{gen}}, \tag{16}$$

where τ_{gen} denotes the lifetime of generated charge carriers, and n_i is the intrinsic carrier concentration defined as:

$$n_i^2 = np = N_C N_V e^{\frac{-E_g}{k_B T}}. \tag{17}$$

The effective densities of states are denoted with N_C and N_V for conduction band and valence band, respectively. E_g is the band gap of the semiconductor, k_B Bolzmann's constant, and T the temperature.

Diodes are only partially depleted at low reverse bias voltage. In such circumstances, the total reverse leakage current can be expressed as the sum of the diffusion current J_s from the non-depleted area and the generation current J_{gen} from the SCR. The leakage current is also affected by other parasitic currents such as surface generation current. This can however be neglected along with other unideal conditions such as tunneling of charge carriers between energy states in the band gap and the series resistance in the junction structure. In particle detectors, the minority charge carrier concentration also remains significantly lower than the density of majority charge carriers, thus excluding a high-injection case.

Consequently, J_{gen} becomes the dominant component of the leakage current when diodes are fully depleted. Hence, the total leakage current of a fully depleted detector can be approximated by Equation 16. Although τ_{gen} depends very weakly on the temperature, the intrinsic carrier concentration n_i is strongly temperature dependent, as evident from Equation 17. Thus, the temperature dependence of the generation current is highly significant.

2.2 Particle Detectors

A diode structure is operated under reverse bias in detecting mode, because detector operation based on diffusion would not be fast enough to separate single signals from each other. Collision events occur in the LHC in 25-ns intervals, and the signals must be read out in each interval. This can only be achieved by reading out the drift current caused by the electric field.

Practical implementations of detectors are usually based on lightly doped bulk material with thin, high-resistivity, and highly doped implantations. This strongly asymmetrical junction can be described with the theory of a one-sided abrupt junction as presented in the previous section. Traditional detectors have mostly been fabricated from n-type bulk silicon. The front side is doped with acceptor-type impurities to create a p^+-type implantation, and a n^+-type implantation forms on the back side as a result of donor doping. Thus, the p-n junction is formed close to the front side of the detector.

During operation the detector is fully depleted by reverse bias. The carriers generated by the incident particles drift under the influence of the electric field to the corresponding nodes of the bias voltage. This is illustrated in Figure 5, that indicates, how the holes drift in the direction of the negative potential and the electrons in that of the positive potential.

The band gap E_g of silicon is 1.17 eV, but additional energy is required to excite electrons from the valence band to conduction band, thus creating electron-hole (e-h) pairs. The band gap of silicon is indirect; therefore, there are changes in

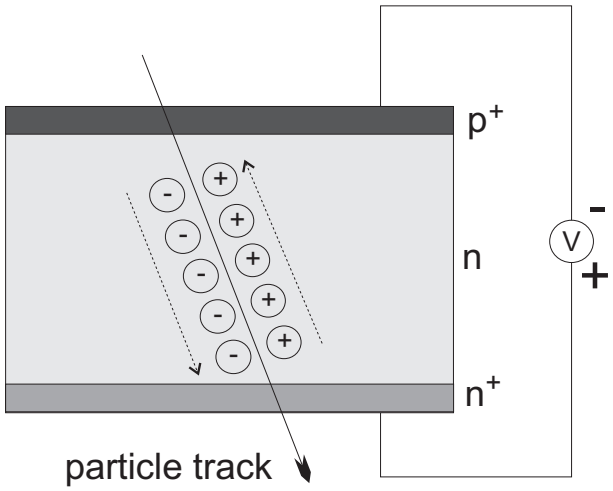

Figure 5: Operational principle of a fully depleted silicon particle detector.

electron momenta when transitions of electrons occur in the band gap structure. Consequently, excited phonons with a certain energy are needed to compensate the momentum changes. Hence, the minimum energy for ionizing silicon diode structures is 3.67 eV at room temperature. [14]

The minimum ionizing particles (MIP) create in a fully depleted 300-μm-thick silicon detector about 22000 electrons, which corresponds to approximately 70 e-h pairs per micron [14]. In order to achieve measurable signals from such level of carrier concentration, the practical implementations of detectors are volume devices. This enables collection of carriers from the entire detector bulk.

Single electrons drifting through a 300-μm-thick detector at an average electric field of 10^4 V/cm are collected in approximately 10 ns, whereas the collection time for holes is approximately 25 ns [14]. The collection times of the charge carriers depend on their drift velocities, which, on the other hand, are determined by the mobilities of electrons and holes, respectively. Thus, the time needed to collect the induced charge carriers varies with temperature as the mobility of both electrons and holes increases with decreasing temperature. Moreover, if the trapping probability of the charge carriers is high, not all induced charge carriers can be collected, and the total amount of the remaining free carriers can be read out in even shorter time than stated above (see Section 3.1).

In HEP experiments two different detector principles are usually applied, pixel and strip detectors. These terms refer to the segmentation of the implantations on the detector surface. The aim of these segmentations is to enhance spatial resolution of the detectors. For example, in CMS strip detectors, 4 x 128 or 6 x 128 detector-long strips are implanted parallel on the substrate. Modern detectors often have AC-coupled read-out electronics because this prevents additional coupling of the leakage current.

3 Radiation Hardness

The tracking detectors in hadron colliders are exposed to significant radiation. To make radiation fluences comparable regardless of the type and energy of the particle beam, they are often expressed as equivalents to fluences of neutrons with the specific energy of 1 MeV. This method is referred to as non-ionizing energy loss (NIEL) scaling and is presented in detail in [15].

For example, in CMS [4], where at the hadron collision point several different elementary particles are created, the accumulated radiation during ten years of operation is expressed as $1.6 \cdot 10^{14}$ cm^{-2} 1 MeV neutron equivalent (n_{eq}) fluence for the innermost strip detectors in the middle of the tracking system. Moreover, the corresponding value is $3.2 \cdot 10^{15}\, n_{eq}/cm^2$ for the innermost pixel detectors at only 4-cm radius from the center of the tracker barrel. Simultaneously, under such radiation, at least the currently installed silicon pixel detectors will most probably deteriorate to an intolerable level in performance [16].

High-intensity radiation damages the crystal structure of the silicon bulk. The incoming energy can displace atoms in the silicon lattice, thus creating vacancies and interstitials. If the incoming particles have sufficiently high energies, multiple crystal defects are created that can cluster and cause larger damaged regions in the bulk crystal as can be seen in Figure 6. It has been observed [17], that the distribution of damage types depends on the type of the incoming particle.

Neutron irradiation results mainly in severe cluster defects, whereas light-energy protons cause mostly individual displacements, i.e., point defects. On the other hand, irradiation with high-energy protons, which fall under the category of fast hadrons, causes both point defects as well as clusters. While the NIEL hypothesis scales the equivalent energy losses well, it needs to be noted that the different distribution of defect types for different types of radiation is not included in the model.

Furthermore, the defects lead to three major effects. First of all, the current leakage

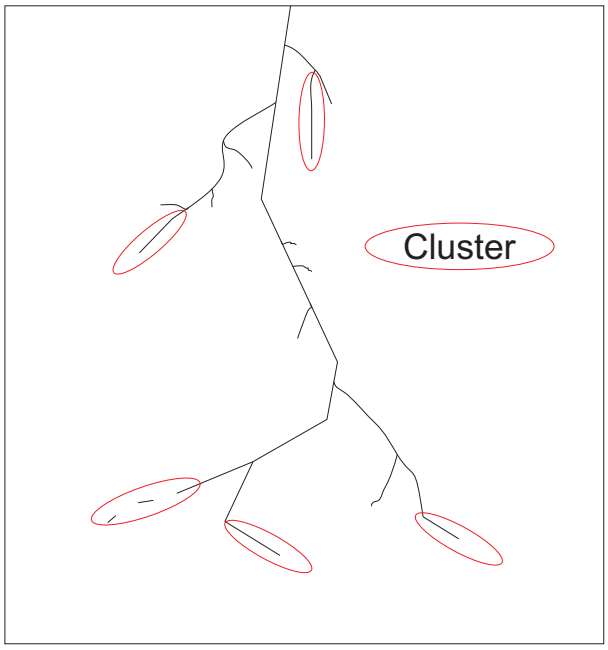

Figure 6: Schematic illustration of damage induced by incoming radiation in a detector crystal.

increases because the crystal defects, that have energy states close to the middle of the band gap, act as generation centers of charge carriers. Second of all, the effective doping concentration N_{eff} changes. The full depletion voltage V_{fd} is proportional to N_{eff}; thus, increasing the absolute value of N_{eff} results in the increase of V_{fd}. Finally, the deep-level energy states of the defects trap free charge carriers. In this case the charge collection efficiency (CCE) decreases, because the charge carriers stay usually trapped for a longer period than the shaping time of the read-out electronics.

Various methods have been investigated to improve the radiation hardness of silicon devices and reduce the unwanted effects caused by the damages. Both the macroscopic effects resulting from radiation induced defects and the most successful approaches for enhancing radiation hardness are discussed in the following sections.

3.1 Effects of Radiation Induced Damage

As explained in Section 2.1, the main source of leakage current in silicon detectors is the generation current in the depletion region. Irradiation defects increase the number of generation centers in the detector bulk, and this leads to growing leakage current. Although the defects are crystallographic, the crystallographic orientation does not influence the increase of the leakage current after proton irradiation, as do not the initial doping concentration or other characteristics of the detector material either. The current growth ΔI is rather proportional to the irradiation fluence as follows [18]:

$$\Delta I = \alpha \Phi_{eq} Vol. \tag{18}$$

Here α is the current related damage rate, Φ_{eq} is the 1-MeV neutron equivalent dose of irradiation, and Vol is the active volume of the detecting device. As noted already in Equation 16, the current is exponentially temperature dependent. Therefore, the analysis of current data requires normalization of the current values to a reference temperature. [18]

It has been concluded in earlier studies [19], that cluster related defects in the silicon bulk act as acceptors as a consequence of hadron irradiation. Therefore, they contribute to the total N_{eff} in the depleted region as negative charges. At higher fluences, the number of defects increases, thus increasing the negative component of N_{eff}, as well. For p-type detectors, which have negative space charge in the bulk to begin with, this results in increase of V_{fd} according to [13]:

$$|N_{eff}| = \frac{2\epsilon_s V_{fd}}{qD^2}. \tag{19}$$

Equation 19 is actually a more general form of Equation 10, when it is assumed that $|V_{fd}| >> |V_{bi}|$. This is the case in practical implementations of detectors, as the depletion voltages of irradiated devices can rise to values around 500 V. Since the limit for the operational voltage is at 500 V in CMS as well as in many other HEP experiments, the increase of the depletion voltage states a real problem.

The effect on n-type detectors is more complex. The space charge in the deple-

tion region in n-type bulk is positive in sign, and the negative contribution of the acceptor-type defects on N_{eff} therefore compensate for the original space charge. At sufficiently high fluences, the defect-induced negative charges overcompensate the positive charges, and N_{eff} inverts to a negative value. This phenomenon is referred to as the space charge sign inversion (SCSI). After the SCSI the type-inverted n-type detector acts as a "p-type" detector with increasing radiation fluences. [18]

The development of the absolute value of the space charge in n-type detectors is illustrated in Figure 7. The figure shows the space charge first inverting and afterwards increasing with the irradiation fluence, when the detector behaves as a "p-type" detector. As noted above, the voltage of full depletion is directly proportional to the effective doping concentration and as such its absolute value shows similar behavior in dependence from the irradiation fluence.

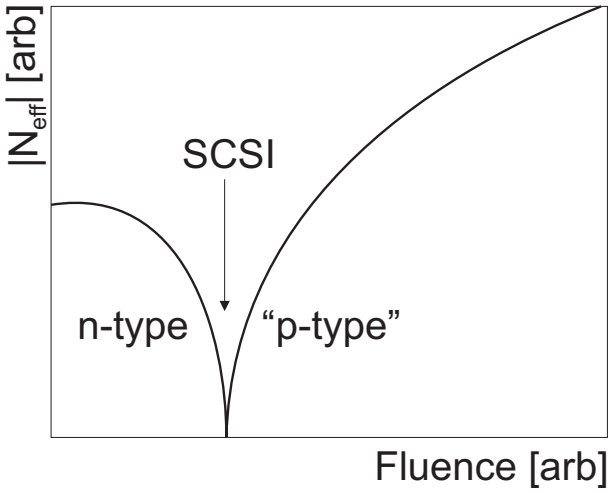

Figure 7: Schematic graph of the effective doping concentration in n-type detectors depending on fluence.

The charge collection efficiency of a detector is significant in harsh radiation environments, because the depletion voltages can rise close or even beyond the highest possible operation voltage. CCE is the ratio of the total collected charge Q and the induced charge Q_0 and it is determined by two factors. For diodes, the geometrical factor CCE_g is simply the ratio of the depletion width and thickness of the detector. Obviously, when the detector is fully depleted, this ratio can be considered to be 1.

As mentioned above, radiation damages cause trapping of charge carriers in deep level states in the detecting volume. Let the trapping induced factor be CCE_t, and thus [20]

$$CCE = \frac{Q}{Q_0} = CCE_g \cdot CCE_t = \frac{W}{D}\frac{\tau_{eff}}{t_{dr}} \cdot \left(1 - e^{-\frac{t_{dr}}{\tau_{eff}}}\right) \tag{20}$$

results for CCE. W is the depletion width of the p-n junction and D the detector thickness. The drifting time and effective trapping time of the charge carriers are denoted with t_{dr} and τ_{eff}, respectively. The effective trapping time equals the generation lifetime in Equation 16 and can be written as [21]:

$$\tau_{eff} = \frac{1}{\sigma_{e,h} v_t N_t}, \tag{21}$$

where N_t is the the density of deep levels and v_t is the thermal velocity. The trapping cross section is denoted by $\sigma_{e,h}$, which determines the tendency of the charge carriers to get trapped in deep level states. The detrapping time, on the other hand, is strongly dependent of temperature [21]:

$$\tau_{detrap} = \frac{1}{\sigma_{e,h} v_t N_{C,V} e^{-\frac{E_t}{k_B T}}}. \tag{22}$$

Here $N_{C,V}$ is the density of states of either the conduction band or the valence band, depending of the type of the detector bulk, and E_t is the activation energy for detrapping.

3.2 Methods for the Improvement of Radiation Hardness

It is possible to use three different approaches to develop more radiation hard detectors. Adding impurity atoms to the semiconductor material on purpose to enhance the radiation hardness is called defect engineering. In addition, device engineering methods can be employed and the operational conditions of the detectors can be varied. For example, the CERN RD39 collaboration emphasizes research in cryogenic operation temperatures of silicon detectors [20].

Zheng Li et al. observed [10], that oxygen content improves the radiation hardness of heavily irradiated silicon. The detailed explanation is that impurity atoms like

oxygen or carbon capture microscopic defects. The oxygen atoms react with the diffusing vacancy defects in the bulk material, forming new complexes of defects and impurities. Carbon reacts with interstitials; unlike oxygen, however, carbon does not show any desirable impact on slowing down the increase of N_{eff}. The CERN RD48 and RD50 collaborations have put extensive effort into research of properties in radiation hard silicon. For example, diffusion oxygenated Float Zone silicon was introduced to the HEP community by the RD48 collaboration [22]; as a result, this material is indeed used in the pixel detectors in CMS and ATLAS.

A reasonable possibility in the category of device engineering is to process the detectors on silicon wafers grown by the magnetic Czochralski method instead of the FZ method [23, 24]. In both methods sufficient semiconductor purity is achieved via the higher solubility of impurities at higher temperatures. The essential difference between the Czochralski and Float Zone methods is the contact to other materials during crystal growth. In contrast to CZ-Si, FZ-Si never comes in contact with other materials during the process. A schematic picture of both crystal growth methods is presented in Figure 8.

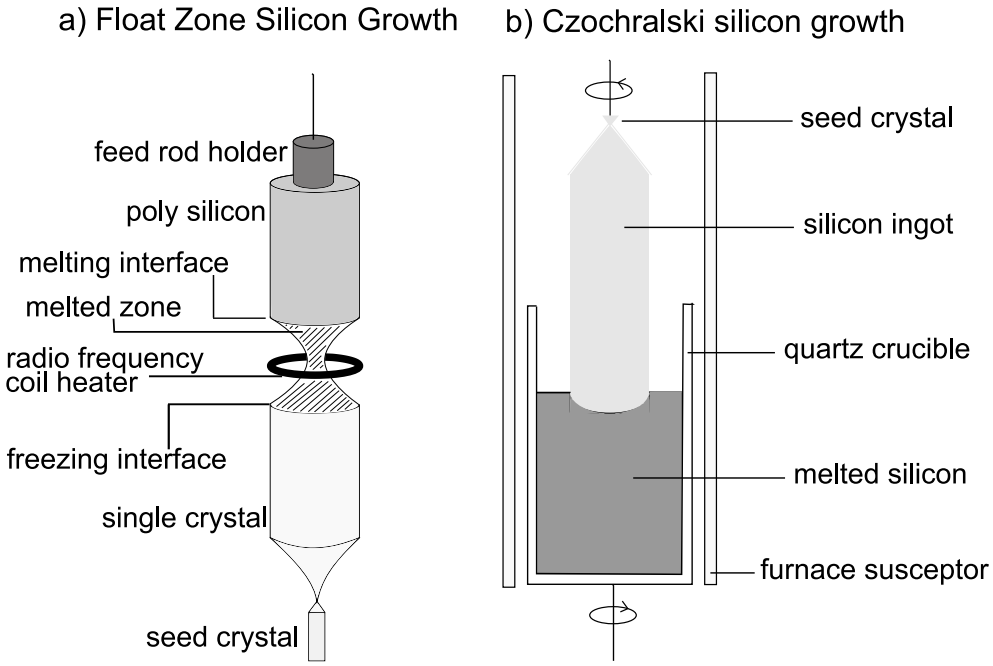

Figure 8: Schematic illustration of Float Zone and Czochralski crystal growth techniques.

In the FZ process, a rod of polycrystalline silicon with a single crystal silicon seed mounted at the bottom is heated by moving the heater upwards starting at the bottom. The melted poly-Si crystallizes again with a single crystal orientation according to the seed. Possible impurity atoms, such as oxygen, have higher solubility in the float zone melt at a higher temperature than in the cooler solid. Thus, the single crystal rod becomes considerably pure in the bottom end where the heating process starts.

However, as the impurities diffuse into the melt during the process, the top end results in a more impure solid that must be cut off. Thus, the process is repeated until the whole rod is sufficiently pure. The end product is considerably pure, and this is the reason for utilizing diffusion oxygenation for FZ-Si to achieve higher oxygen concentration for the purpose of enhancing radiation hardness.

During the Czochralski process, melted silicon is held in a rotating quartz crucible in a furnace. An ingot, which is originating from a single crystal seed and rotating in the opposite direction than the crucible, is pulled out of the melt. The molten silicon solidifies along the crystal structure of the seed. During this process, oxygen and other impurities from the crucible are released into the melt and solidify into the ingot, as well. However, the same principle holds as during the FZ process: impurities are more soluble in the high temperature melt than in the solidifying rod, thus guaranteeing sufficient purity.

Applying a magnetic field during the growth process enables controlling of the fluctuations of the impurities, thus causing a more homogeneous impurity distribution in the final silicon wafers. Czochralski silicon is the dominant semiconductor material in electronics industry and more cost-efficient than traditional FZ-Si. After significant development, the microelectronics industry at present can also provide high-resistivity MCZ silicon wafers, and the oxygen concentration can be well adjusted during fabrication of the wafers.

Another approach currently being investigated is device engineering, namely to process n^+-p-p^+ detector structures instead of traditional p^+-n-n^+ structures [25, 26].

The p-type detectors show comparable electrical properties to those of n-type detectors. Furthermore, the behavior of the full depletion voltage has been observed to be less sensitive to harsh irradiation [25]. In addition, in such a detector, the signal is read from the n^+-type implantation; i.e., the charge carriers contributing to the signal are electrons. Electrons have a drift time of approximately 10 ns through a 300-μm detector. This is more than twice as fast as the drift time of holes in n-type detectors; i.e., the mobility of electrons is significantly higher than that of holes. In addition, electrons have lower trapping probability than holes; this leads to higher charge collection efficiency, as well.

A significant difference between n-type and p-type bulk is the occurrence of space charge sign inversion. In contrast to n-type, p-type detectors do not show a tendency to SCSI that was explained in Section 3.1. Thus, the p-n junction remains close to the read-out electrode in the p-type case, and this leads to a desirable effect that relates to signal quality. The electric field in real segmented and heavily irradiated detectors is not linear as that through an ideal diode [27]. The geometry of a detector determines the weighting of the electric field [28]. The weighting field effect causes the charge carriers to induce most charge close to the segmented side of the detector and in the corresponding read-out contact. As the collected charge consists of electrons with the advantages described above, using n^+-p-p^+ structures can result in higher charge collection.

The closer the strong electric field is to the segmented side of the detector, the better the signal is localized. This is a clear advantage, as the silicon detectors are mainly used in tracking systems. Consequently, it is profitable to have the p-n junction and thus the strongest electric field close to the n^+-read-out electrode.

The shape of the electric field provides information about both the space charge of the bulk as well as the behavior of the charge carriers. These, in turn, have an impact on practically all the parameters for radiation hardness. Thus, it can be concluded, that it is of importance to analyze the electric field of silicon detector structures in radiation hardness studies.

3.3 Annealing

The irradiated silicon detectors are very sensitive to heat treatment. After a long-time exposure to room temperature, or at sufficiently high temperatures, the microscopic defects are annealed in the crystal. The annealing mechanisms are migration, complex formation and complex dissociation of the defects [18].

It has been observed, that annealing during a relatively short time has radiation hardness improving effects, whereas relatively long-term annealing impairs the radiation hardness of detectors. Therefore, the effects of heat treatment are divided into two categories: beneficial and reverse annealing. Both of these annealing types depend on the irradiation fluence, annealing time, and annealing temperature. Previous studies [18] have shown that exposure of irradiated silicon detectors to room temperature for 55 h corresponds roughly to the exposure of the detectors to 80℃ for 2 min in the range of beneficial annealing. For reverse annealing, 2 min at 80℃ approximately correspond to 10 days at room temperature.

The factor α from Equation 18 has been observed to decrease constantly with the annealing time [29]. This is an expression for the change of the leakage current generation. With very small α the leakage current saturates to a certain level. The reduction of α can be clearly observed in Figure 9.

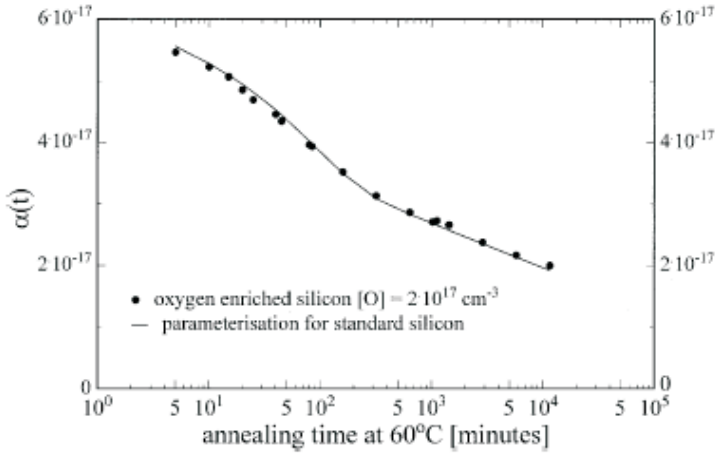

Figure 9: Current related damage rate α as a function of cumulated annealing time at 60℃. [30]

On the other hand, observations have been made of decreasing depletion voltages during the first phase of annealing followed by an increase of the V_{fd} absolute values in the second phase. This behavior has also lead to the terms of beneficial and reverse annealing. As described in Section 3.1, the changes in the depletion voltages depend on the changes of the effective doping concentrations. The change ΔN_{eff} is a sum of three components. In addition to the completely fluence dependent component, the components describing beneficial and reverse annealing are significant, as well. The behavior of ΔN_{eff} is illustrated in Figure 10.

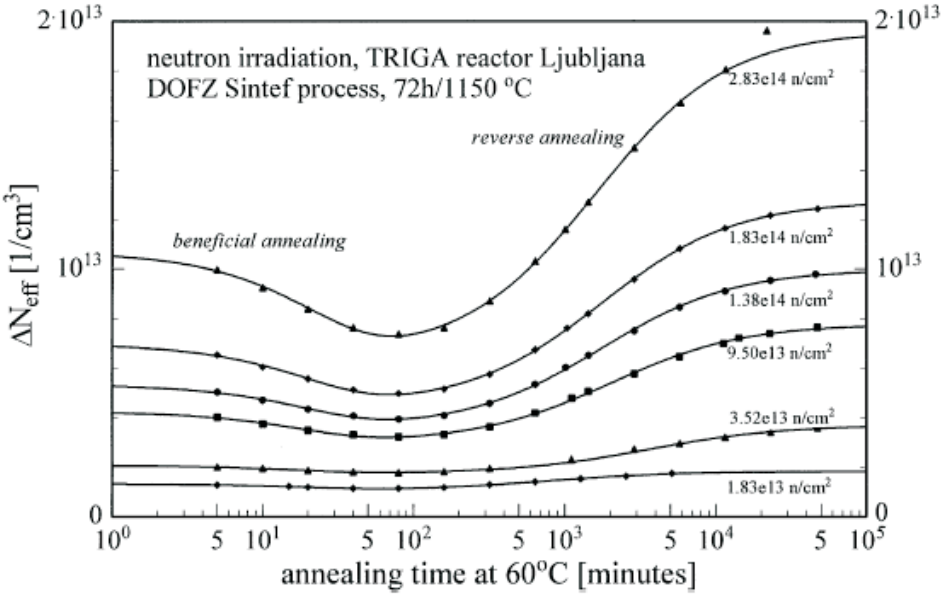

Figure 10: Change of effective doping concentration ΔN_{eff} during isothermal annealing at 60℃ of oxygen enriched silicon detectors irradiated with different neutron fluences. [30]

Creation of acceptor-type defect complexes can be used as an explanation for the increase of $|N_{eff}|$ and $|V_{fd}|$, which becomes evident especially during reverse annealing. During beneficial annealing, however, the acceptor type crystal defects are annealed. According to Equation 11, the effective doping concentration is the difference between the donor and the acceptor concentration. A majority of acceptor-type charge density, as in p-type devices, results in a negative effective doping concentration. With the annealing of the acceptors, N_{eff} becomes less negative in p-type detectors. Consequently, the absolute value of the depletion voltage decreases with

the reduction of $|N_{eff}|$. The same phenomenon of beneficial annealing can be observed in n-type detectors after space charge sign inversion.

4 Transient Current Technique Measurements

Analog to detector operation, bias voltage is applied during TCT measurements. The principle of TCT measurements is to observe the signal created by drifting charge carriers in the silicon detector bulk. The free charge carriers are generated in consequence of illuminating the detector by red laser light. If the front side implantation of the reverse-biased diode is illuminated, the charge carriers, that are collected from the front side, drift to the contact faster than the read-out electronics can respond. On the other hand, the carriers opposite in sign drift through the whole detector to the back side. This transient current is the measured signal.

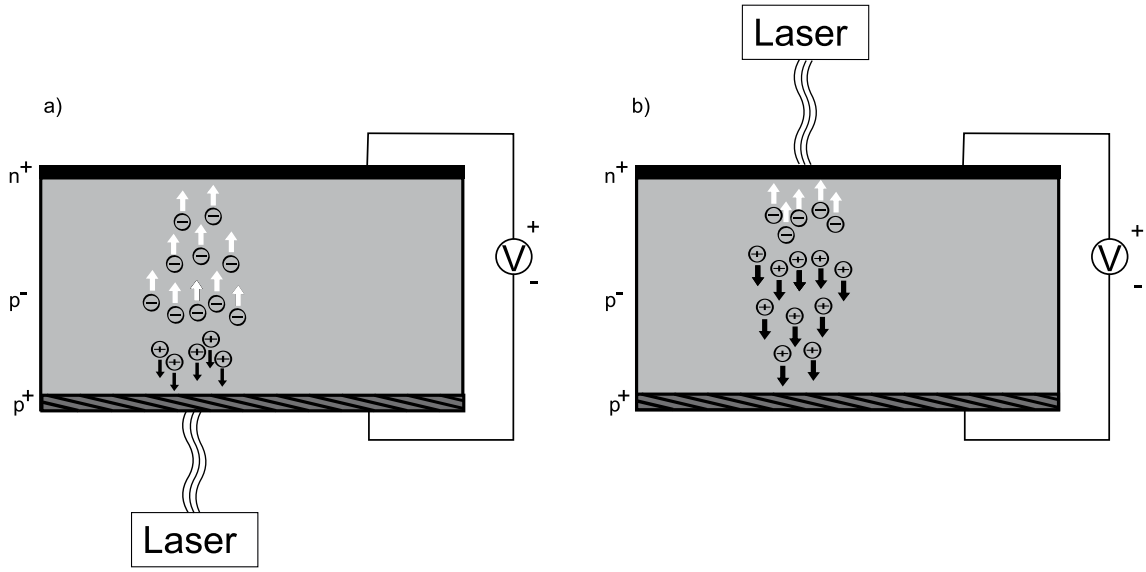

Figure 11: a) The back side of a n^+-p^--p^+ diode is being illuminated, and the resulting TCT signal comes from electrons. b) Illumination of the front side of the same diode structure results in a TCT signal caused by holes.

If a reverse-biased detector is being illuminated from the front side, the measured signal originates from the charge carriers equal in sign to the majority carriers in the bulk as presented in Figure 11. The figure shows how the TCT signal in a p-type detector is caused by holes when illuminated from the front side. Illumination from the back side results in a signal originating from electrons.

It is possible to extract the response of the detector to MIP's by performing TCT measurements on diodes illuminated by infra red lasers. Photons with a wavelength

in the infra red region have an energy lower than the band gap of silicon. Thus, the IR photons penetrate considerably deeper into the 300-μm detector bulk than photons in the red wavelength region. As as result, the generation of e-h pairs remains moderate but homogeneous through the entire bulk. This leads to a TCT signal caused by both charge carriers, electrons and holes, as is the case with real MIP's.

The benefits of TCT measurements with IR illumination become evident in the determination of V_{fd} and CCE. More reliable determination of the state of full depletion is possible, when the charge carriers are generated homogeneously through the device. Otherwise, with the possibility of maximum carrier densities close to the electric field maximum, the majority of charge carriers could be collected before the whole detector is depleted.

The MIP simulation is advantageous when considering examination of the charge collection efficiency, as well. As mentioned in Section 3.1, CCE is the relation of the collected charge Q and the originally induced charge Q_0 in a detector. With the infra-red TCT measurements, Q_0 can be set equivalent with the collected charge in a non-irradiated detector, i.e., $CCE = 1$. This is assumed to correspond to 22000 electrons induced by a single MIP in a 300-μm thick silicon detector.

4.1 Determination of the Electric Field Distribution, Full Depletion Voltage, and Effective Trapping Time

According to Ohm's Law the transient current is directly dependent on the electric field between the front and back side of the detector:

$$\vec{\mathbf{J}} = \sigma \cdot \vec{\mathbf{E}}. \tag{23}$$

$\vec{\mathbf{J}}$ is the current density, σ the conductivity, and $\vec{\mathbf{E}}$ the electric field. As mentioned previously, the diffusion component caused by the carrier concentration gradient can be neglected when considering TCT measurements. Thus, the drift current is dominant, and the current density in Equation 23 can be written for electrons and

holes as follows [13]:

$$\mathbf{J}_n = q\mu_n n\mathbf{E}, \tag{24}$$

$$\mathbf{J}_p = q\mu_p p\mathbf{E}. \tag{25}$$

Here, q is the elementary charge, n the charge concentration of electrons and p that of holes. The mobilities for electrons and holes are denoted by μ_n and μ_p, respectively.

From this follows that the shape of the TCT signal resembles the shape and location of the electric field. The electric field is strongest at the location of the actual p-n junction. There, the drift current is at its highest, as well, since it is proportional to the electric field as can be seen in the equations above. The junction is usually located at the interface of the bulk and the implantation opposite in sign. If the signal is measured from the side where the junction is located, the TCT signal is descending. If the junction has moved to the back because of space charge sign inversion, the measured signal from the front side is ascending. This is illustrated in Figure 12. A clear sign of SCSI is thus an ascending TCT signal as in Figure 12b). Obviously, this leads to conclusions about the sign of the space charge, as well, when the junction structure of the detector is known.

In addition to the determination of the sign of the space charge and the electric field distribution, it is also possible to extract the full depletion voltage V_{fd} and the effective trapping time τ_{eff} in the bulk from the TCT measurement data. The transient current measurement allows to obtain directly the amount of collected charge by integrating the current signal over time. The charge collection also rises steeply at increasing voltages until the full depletion voltage.

If trapping and detrapping of the charge carriers occur within the current integration time, the amount of collected charge saturates at voltages above V_{fd}, e.g., at full depletion. If the shaping time of the read-out electronics is as short as in the LHC experiments, detrapping of the captured charge carriers does not occur within the RC time constant of the read-out. Thus the total induced charge is not collected, and the saturation of the charge collection does not become visible in a charge

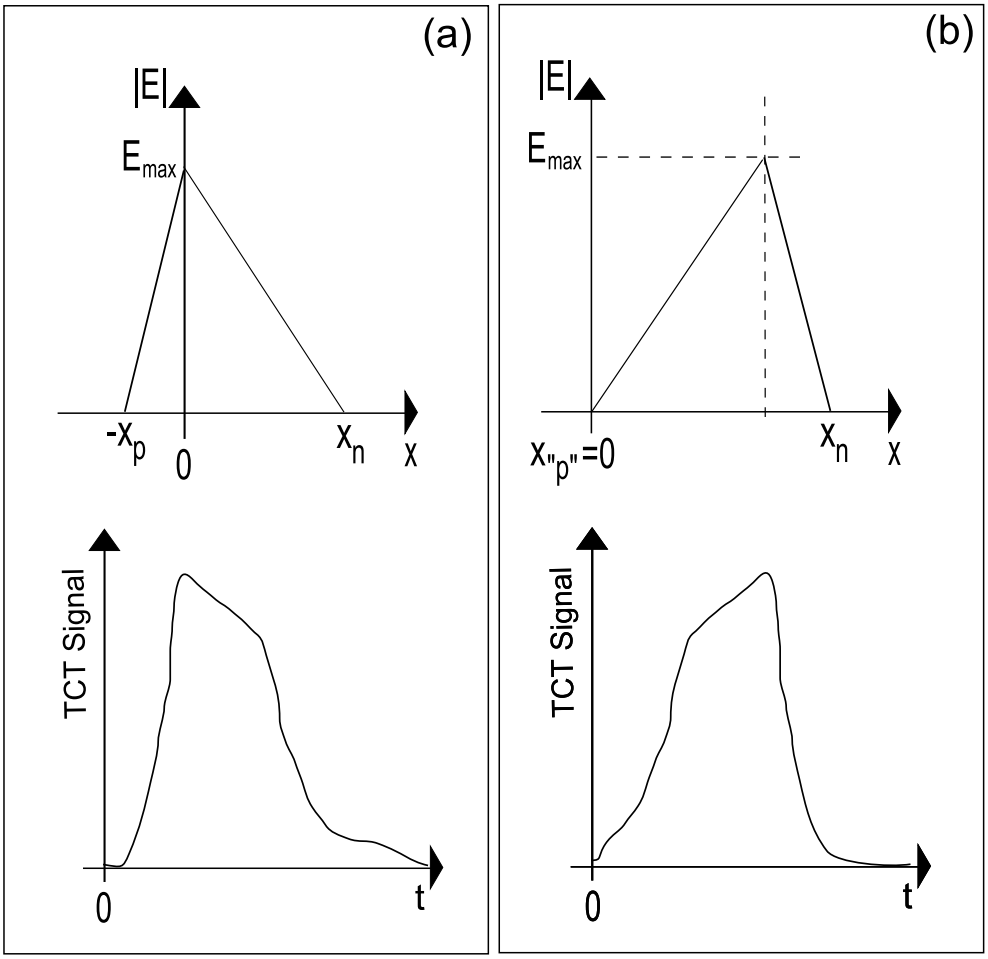

Figure 12: a) A p^+-n-n^+ structure with the maximum electric field at front provides a descending transient current. b) A type-inverted p^+-n-n^+ structure has its electric field maximum at the back side of the diode, and the transient current is ascending.

collection measurement graph. Instead, the graph continuously shows increasing charge collection; however, with a reduced slope at voltages $|V| > |V_{fd}|$. [31]

The value of the depletion voltage can be determined by a graphical method from a graph showing the collected charge as a function of applied bias voltage as illustrated in Figure 13. The intersection of the linear fittings of the high and small slope regions provide the voltage of full depletion.

The method for the determination of the effective trapping time τ_{eff} is presented in the following according to [31]. The transient current $i(t)$ in the detector caused by

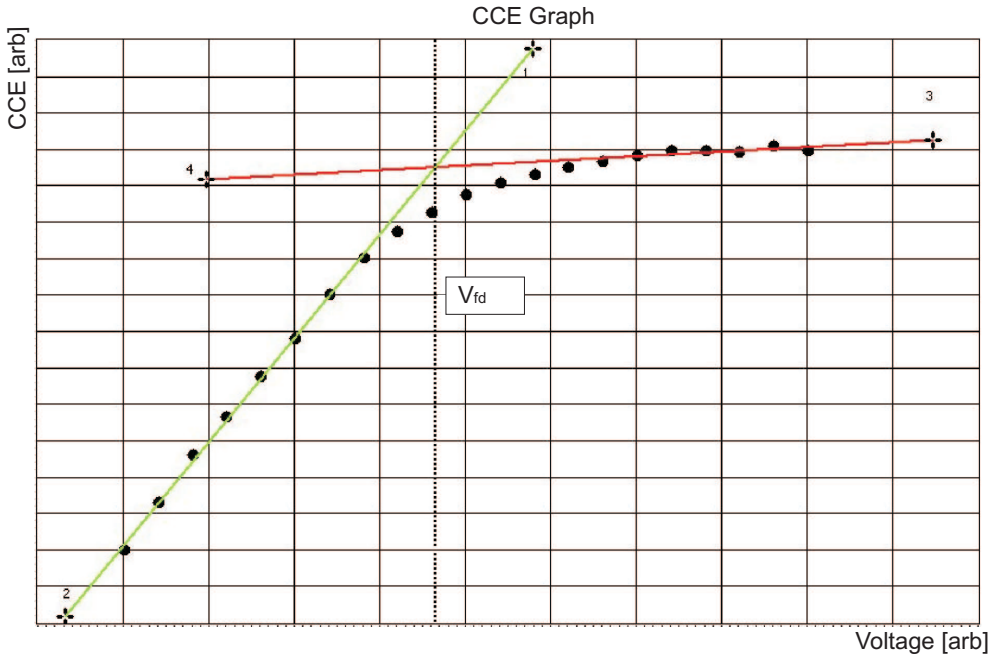

Figure 13: Obtaining V_{fd} from a CCE graph.

one charge carrier can be expressed with the help of Ramo's theorem [32]:

$$i(t) = qv_{dr}\mathbf{E}_v = q\mu E(x)\frac{1}{D}\,, \tag{26}$$

where q is the elementary charge, v_{dr} the velocity of the charge carrier and $\mathbf{E}_v$ is the electric field caused by unit potential in the location of the carrier. The right hand side of the equation introduces the carrier velocity as a product of carrier mobility μ and electric field $E(x)$. $\mathbf{E}_v$ is replaced by the inverse value of the thickness D of a non-segmented pad detector, i.e., a diode.

When considering the total transient current $I(t)$, the carrier concentration factor must be added to Equation 26. The carrier concentration, however, does not hold the constant value of injected carriers but decreases depending on τ_{eff} [31]. The dependence for the electron concentration n is written as:

$$n = n_0 \cdot e^{-\frac{t_{dr}}{\tau_{eff}}}, \tag{27}$$

where n_0 is the injected carrier density, and t_{dr} is the drift time of the carriers through the diode. The exponential term above can be used to correct the measured

transient current, and $I(t)$ results in:

$$I(t) = n_0 \frac{q\mu E(x)}{D} e^{-\frac{t}{\tau_{eff}}}. \tag{28}$$

This expression for the transient current indeed equals the current that can be deducted from the current density in Ohm's law (Equations 24, 25), except for the exponential correction added due to trapping.

The collected charge can be calculated by integrating the transient current over time:

$$\begin{aligned} Q &= \int_0^{t_{dr}} I(t)dt \qquad (29) \\ &= \frac{Q_0 v_{dr}}{D} \int_0^{t_{dr}} e^{-\frac{t}{\tau_{eff}}} dt \\ &= \frac{Q_0 v_{dr}}{D} \tau_{eff} \left(1 - e^{-\frac{t_{dr}}{\tau_{eff}}}\right) \\ &= \frac{Q_0 W}{D} \frac{\tau_{eff}}{t_{dr}} \left(1 - e^{-\frac{t_{dr}}{\tau_{eff}}}\right). \qquad (30) \end{aligned}$$

Here, the depletion width W results from $v_{dr} t_{dr}$. It has also been assumed that the electric field through the non-segmented pad-detector is constant, thus causing the transient current to remain independent of location x. When dividing equation 30 by Q_0, the result is indeed the charge collection efficiency as demonstrated in Equation 20.

Let us assume, that the charge collection efficiency depends only on the trapping factor at full depletion of the detector as the depletion width W equals the device thickness D. Then, with the right value for τ_{eff} inserted in the current integral, the corrected amount of collected charge stays constant for voltages above V_{fd}. Hence, searching a value, that forces the charge collection graph to reach a plateau typical for saturation, results in an accurate value for the effective trapping probability.

Equation 30 can be used to evaluate τ_{eff} with the collected charge Q being the integral over time of the measured current transient. If the detectors have been irradiated with a modest particle fluence ($< 2 \cdot 10^{15}\, n_{eq}/cm^2$), the effective trapping time has a significantly larger value than the drift time of the charge carriers ($\tau_{eff} \gg$

t_{dr}). Thus following approximation of Equation 30 becomes valid for the collected electrons [20]:

$$Q \approx Q_0 \frac{W}{D}(1 - \frac{1}{2} \cdot \frac{\tau_{eff}}{t_{dr}}). \tag{31}$$

After extremely high radiation ($\sim 10^{16}\, n_{eq}/cm^2$) or long time annealing, the effective trapping time is considerably shorter than the drifting time through the device, and the charge carriers are captured in traps within the measurement time window. Under such conditions ($\tau_{eff} \ll t_{dr}$), Equation 30 for electrons simplifies to [20]

$$Q \approx Q_0 \frac{W}{D} \frac{\tau_{eff}}{t_{dr}}. \tag{32}$$

4.2 Measurement setup

The TCT measurement setup used in this thesis project was designed and built by the CERN RD39 Collaboration [33]. A schematic overview of the setup is presented in Figure 14, and a photograph of the practical measurement equipment is shown in Figure 15. The sample is placed on a cold finger inside a vacuum chamber. The vacuum is created with a turbo pump and a Leybold helium stirling cooler is used for the cooling of the chamber. The bias voltage from a source meter unit is applied to the sample diode through a coaxial copper transmission line designed for cryogenic applications in particular.

The diodes are mounted with carbon adhesive tapes on ceramic plates. The contact between the diode and the transmission line is realized by soldering a gold pin from the back side of the ceramic plate into an opening in the middle of the plate. This pin can be directly connected to the coaxial cable. The ceramic plates have a patterned gold metallization, and the pad contact on the front side of the sample diode along with the guard ring are bonded to the metallization. The contact between the gold-plating and the copper cold finger is established by four copper springs.

As the back sides of the diodes are attached to the plates firmly, only the front side of the sample can be illuminated with a laser diode from Advanced Laser Diode

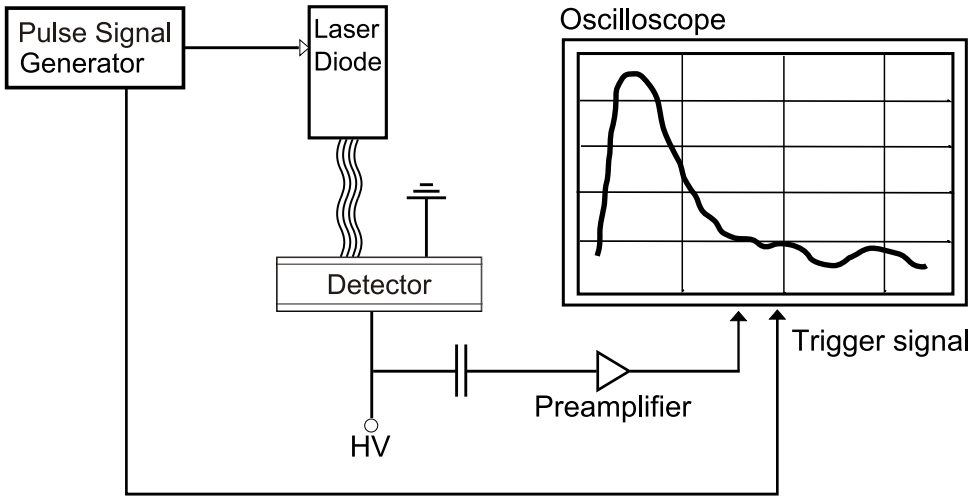

Figure 14: Sketch of the principle of the TCT measurement setup.

Systems A.L.S. GmbH. The used wavelengths are in the red region (678 nm) and infra-red region (1060 nm), and the pulse length of the lasers is about 30 ps. The laser diodes were operated in all measurements with a trigger rate of 50 Hz and an output efficiency of 70% with the maximum optical power being 250 mW. The same trigger rate was also used for triggering the Le Croy Wavepro 7K 3 GHz oscilloscope, which reads out the output signal. The output signal is transmitted to the oscilloscope over the same coaxial cable as the bias voltage and amplified before the plug-in. The gain is 600, and the impedance of the oscilloscope equals 50 Ω. The measurement settings and data aquisition are handled by a user interface based on LabView.

4.3 Samples and Measurements

This study covered the examination of altogether 11 different diodes. The diodes have a basic double-sided p^+-n-n^+ or n^+-p-p^+ pn-diode structure. The component area is surrounded with a guard ring to define the active volume precisely and prevent skewing of the leakage current measurements. With no guard ring, the electric field could reach the dicing edge of the sample. Then, large external currents could be pulled into the diode.

The contact pad on the front side has an opening in the middle, thus enabling direct

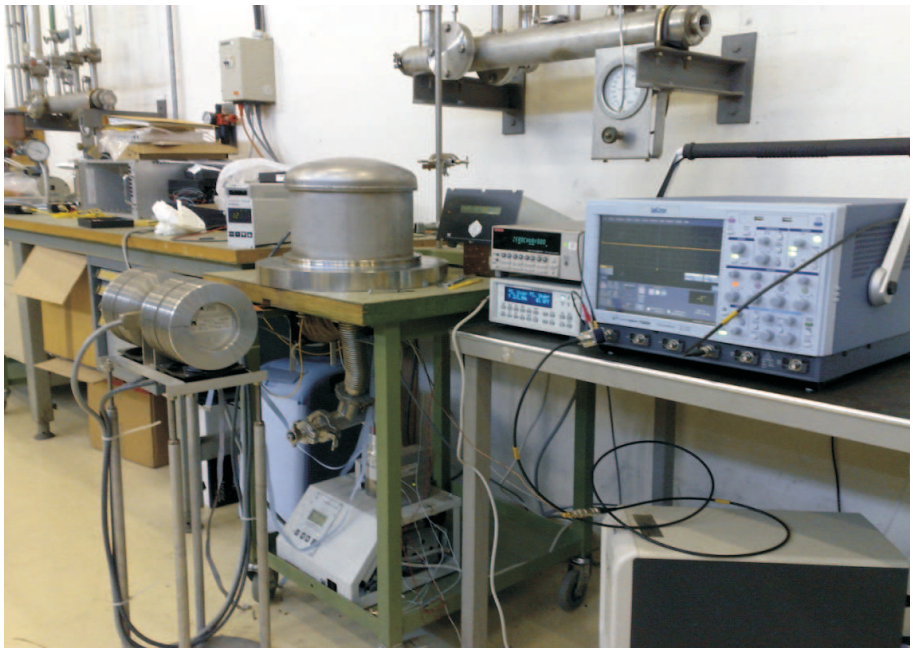

Figure 15: The TCT measurement setup of the CERN RD39 Collaboration.

illumination of the diode. The opening in the pad, the guard ring, and the bonding wires can be seen in Figure 16a), where a diode is glued on the ceramic plate. The size of the diode samples is 8 mm x 8 mm, although the active detecting volume is sized 5 mm x 5 mm. Figure 16b) is a photograph of a processing mask of the diodes, which shows the pad contact on the front side of the diode as well as the guard ring located between the active detector and the edge of the sample.

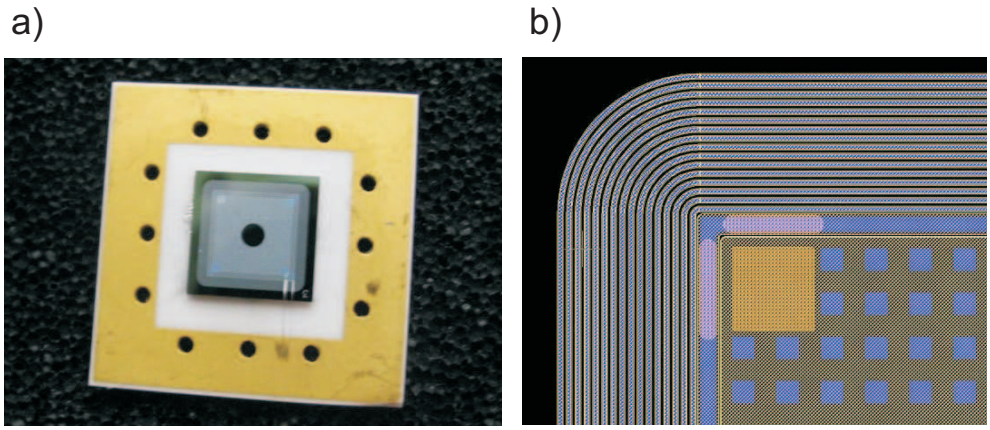

Figure 16: a) A diode sample on a ceramic plate prepared for TCT measurements. b) Photograph of a corner in the processing mask. The pad contact opening and the guard rings are clearly visible.

The experiments included investigation of both Float Zone silicon samples and magnetic Czochralski silicon samples. The FZ diodes have been fabricated at Centro Nacional de Microelectrónica (IMB-CNM, CSIC) in Barcelona, Spain. They have been provided by the CERN RD50 Collaboration. The MCZ diodes have been manufactured in the clean room facilities of TKK Micronova in Espoo, Finland. All three FZ-Si diodes were processed from n-type bulk. On the other hand, p-type as well as n-type bulk were represented among the MCZ-Si diodes. Four diodes of each MCZ type as well as the three FZ diodes were exposed to different doses of proton radiation. The energy of the protons equaled 23 GeV. The irradiation was carried out at the CERN Proton Synchrotron (PS). Table 1 presents the different radiation fluences and the according samples.

Table 1: The proton irradiation fluences, the neutron equivalent doses, and corresponding sample names.

Fluence $[23\,GeV\,p/cm^2]$	Fluence $[1\,MeV\,n/cm^2]$	MCZ n-type	MCZ p-type	FZ n-type
$1.6 \cdot 10^{14}$	$9.92 \cdot 10^{13}$	n-61	p-50	F-32
$9.7 \cdot 10^{14}$	$6.014 \cdot 10^{14}$	n-58	p-55	F-42
$1.3 \cdot 10^{15}$	$8.06 \cdot 10^{14}$	n-57	p-57	F-70
$2.4 \cdot 10^{15}$	$1.488 \cdot 10^{15}$	n-56	p-61	F-81

Three different measurements at two temperatures were performed on all samples. Before the start of the cooling, the pressure in the vacuum chamber was pumped down to at least $1.0 \cdot 10^{-3}$ mbar. First, TCT measurements were carried out at 240 K under illumination by the infra-red laser. The scanned bias voltage range covered voltages from zero to 500 V with a step size of 25 V.

If the collected charge saturated within the scanned voltage range, the value for the full depletion voltage V_{fd} was obtained from the charge collection efficiency graph as shown in Figure 13. A similar measurement was completed with a laser in the red light region at temperatures 220 K and 240 K. The extracted depletion voltage was used as a set point approximately in the middle to adjust the voltage range accordingly. In addition, current-voltage measurements were executed at both temperatures.

After examination of all samples, the n- and p-type MCZ samples with the irradiation dose of $9.7 \cdot 10^{14}$ p/cm^2 were chosen for a further annealing experiment. Also the behavior of the FZ sample with the dose $1.3 \cdot 10^{15}$ p/cm^2 after annealing was examined for comparison. The annealing experiment included the annealing of the samples at 80℃. Each of these samples was annealed separately in six steps. The variable in these steps was the annealing time according to the recursive rule $t_{n+1} = 2t_n$ with n running from 1 to 6 and annealing time t_1 for the first annealing step being 4 minutes. From this follows the accumulated annealing time of 252 minutes for each sample. The cumulative annealing times and those of each step are summarized in Table 2. After every annealing step, the samples were subjected to the same TCT and I–V measurements as described above for all diode samples before annealing.

Table 2: Cumulative annealing times and those of each step.

Annealing times [min]						
Single step	4	8	16	32	64	128
Cumulative	4	12	28	60	124	252

5 Results and Discussion

Results from the conducted measurements are organized in the following way. First, voltages of full depletion are extracted from MIP measurements, and leakage current values corresponding to the depletion voltages result from I–V measurements. Second, the electric field of the diodes is examined with the help of TCT measurements. At last, annealing behavior of different types of diodes is investigated, as well, with the aforementioned methods.

In general, the results lead to the conclusion that MCZ-Si diodes withstand both irradiation as well as annealing better than FZ-Si diodes when judged by parameters, such as depletion voltage or leakage current. Both types of MCZ based diodes show more preferable performance at 220 K than at 240 K, as the TCT signal strength, for example, is generally higher and the leakage currents lower at the lower temperature. The values resulting for depletion voltages before and after annealing as well as leakage currents after annealing tend to be lower for the p-type MCZ diode samples than for the n-type MCZ samples. Low values for these parameters are as well desired in detector operation in HEP experiments, as well.

5.1 Voltages of Full Depletion and Leakage Currents

The voltages of full depletion V_{fd} were determined from the TCT measurements executed under excitation by a 1060-nm laser at 240 K. The graphical method explained in Section 4.1 was utilized to extract the values for V_{fd}, if the rise of charge collection saturated; i.e., the diode was fully depleted, within the scanned voltage range of 500 V. None of the samples with the highest irradiation dose equivalent to $1.5 \cdot 10^{15} \quad 1\,MeV\,n_{eq}/cm^2$ was fully depleted at a voltage below 500 V. The resulting depletion voltages from the measurement are summarized in Table 3.

The absolute values of the depletion voltages are clearly lower in samples processed from magnetic Czochralski silicon than in float zone diodes. Furthermore, as opposed to the MCZ samples, the FZ-Si diodes did not deplete at a reverse bias below

Table 3: V_{fd} values in [V] determined at a temperature of 240 K.

Dose [$23\,GeV\,p/cm^2$]	MCZ n-type	MCZ p-type	FZ n-type
$1.6 \cdot 10^{14}$	168.3	-57.2	119.1
$9.7 \cdot 10^{14}$	252.3	-197.8	279.0
$1.3 \cdot 10^{15}$	310.8	-269.1	n.d.
$2.4 \cdot 10^{15}$	n.d.	n.d.	

500 V, if they were irradiated with a higher fluence than that corresponding to $6.01 \cdot 10^{14}$ $1\,MeV\,n_{eq}/cm^2$. The lowest absolute value of the depletion voltage was determined for the MCZ p-type sample for each irradiation fluence. This is illustrated in Figure 17, as well.

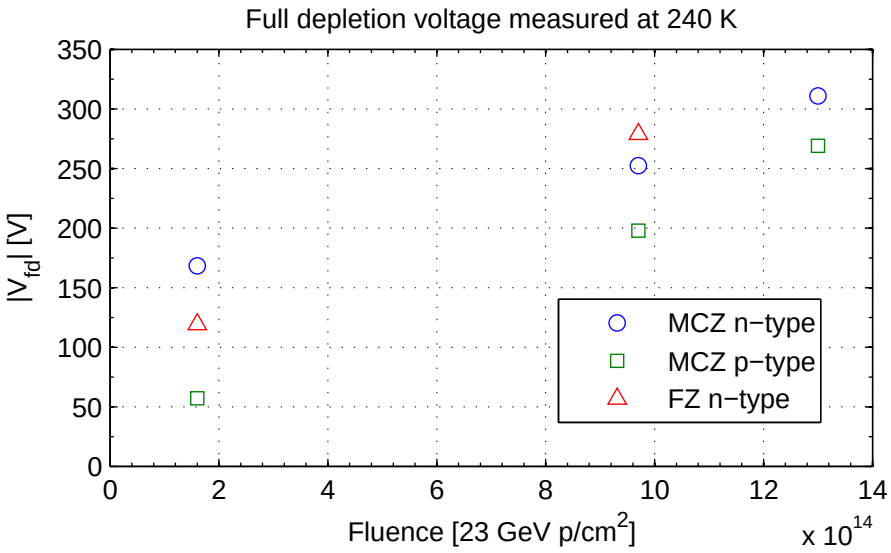

Figure 17: Obtained V_{fd} values for different diode types in dependence of fluence.

Table 4: I_{leak} values in [μA] measured at a bias voltage equaling V_{fd} and a temperature of 240 K.

Dose [$23\,GeV\,p/cm^2$]	MCZ n-type	MCZ p-type	FZ n-type
$1.6 \cdot 10^{14}$	-0.162	0.175	-0.310
$9.7 \cdot 10^{14}$	-0.790	0.898	-1.235
$1.3 \cdot 10^{15}$	-1.803	1.505	n.d.
$2.4 \cdot 10^{15}$	n.d.	n.d.	

The current-voltage measurement at the temperature of 240 K provided the value of the leakage current at a voltage equaling V_{fd}. The results are presented in Table 4.

While both types of MCZ-Si diodes show similar absolute values for the leakage current, the values for the FZ-Si diodes are clearly higher than those for the other samples. This could be expected, as the depletion voltage values for the FZ-Si samples rose clearly above those of the MCZ-Si samples.

5.2 TCT Characterization

TCT measurements were performed on all samples (see Table 1) under illumination of a red ($\lambda = 678$ nm) laser. The results for each diode type with different irradiation fluences are presented in the following. The TCT signals are measured from fully depleted diodes. If the diodes did not deplete at a voltage smaller than 500 V, the signal at a bias voltage of 500 V is shown. A comparison of the MCZ and FZ samples is also included at the end of this section.

TCT signals measured from fully depleted n-type and p-type MCZ-Si diodes can be seen in Figures 18 and 19, respectively. Visual inspection reveals for the n-type samples a better signal to noise ratio (SNR) than for the p-type samples. In principle, the widths of the signals show the drifting time of the charge carriers through the device bulk. Typical values for drifting times through a standard 300-μm silicon device are about 10 ns for electrons and 25 ns for holes. The signal widths of the detectors irradiated with the smallest fluence stay clearly below these values both for electrons in the n-type diode as well as for the holes in the p-type sample.

Furthermore, with increasing irradiation dose, the signals become more narrow as can be seen in the figures. The difference in width between the the widest and most narrow peaks is 2–3 ns for the n-type samples at both temperatures. The difference is approximately 7 ns for the p-type samples, although the difference seems lower at 220 K than at 240 K.

The reason for the narrow signals is that the trapping probability in a silicon detector increases with the radiation exposure. Thus, the charge carriers travelling the longest distance through the device get trapped before reaching the read-out. This results in a smaller signal width.

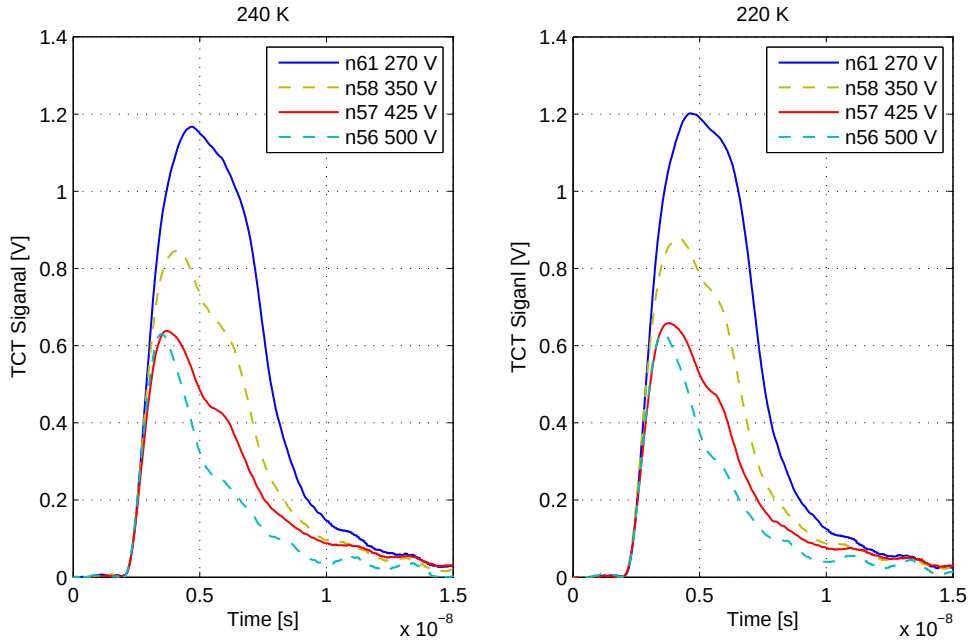

Figure 18: TCT signals of the n-type MCZ-Si samples at a voltage $V \approx V_{fd} + 100V$ or, if $V_{fd} \geq 500V$, $V = 500V$.

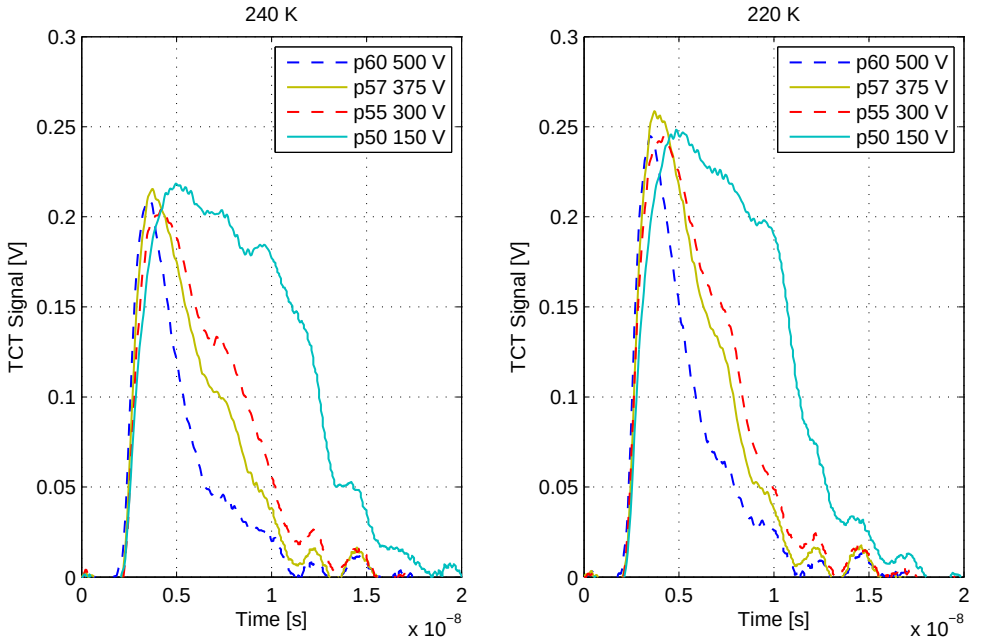

Figure 19: TCT signals of the p-type MCZ-Si samples at a voltage $V \approx V_{fd} + 100V$ or, if $V_{fd} \geq 500V$, $V = 500V$.

The TCT signals measured at 220 K are generally more narrow than those measured at 240 K. This can be explained by the electron and hole mobilities that depend strongly on temperature. Decreasing the measurement temperature by 20 K results in higher mobilities for both electrons and holes. As a result, the charge carriers are collected faster and the signal width decreases.

Another effect caused by trapping can be observed in the signal shapes. MCZ-Si detectors with n-type bulk usually experience SCSI at a fluence in the order of magnitude of 10^{14} $1\,MeV\,n_{eq}/cm^2$. Thus, after sufficient irradiation, the TCT signals should change their shape from descending to ascending according to the electric field distribution. However, our results show only descending signals. It can be assumed for the samples with the higher irradiation fluences, that the trapping has narrowed the signals to an extent, when the ascending part of the signal, and thus the location of the shifted p-n junction, is not visible anymore.

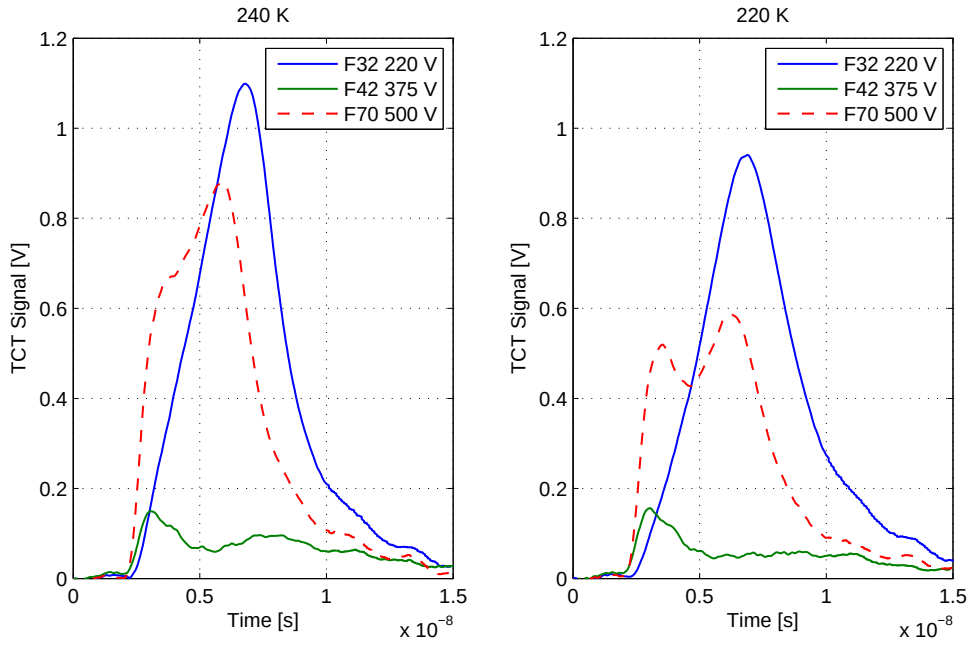

Figure 20: TCT signals of the FZ-Si samples at a voltage $V \approx V_{fd} + 100V$ or, if $V_{fd} \geq 500V$, $V = 500V$.

Figure 20 illustrates the TCT signals measured from the n-type FZ-Si diodes. Measurements of sample F-32 ($1.6 \cdot 10^{14}$ $23\,GeV\,p/cm^2$), which has been exposed to the

smallest irradiation dose, result in a shifted peak compared to all other measurement results presented in this study. This may be caused by the SCSI induced already after lower fluences of irradiation. The double peak effect can be clearly observed in the highly irradiated sample F-70 ($1.3 \cdot 10^{15}$ $23\,GeV\,p/cm^2$) at 220 K. Double-peak formation is caused by trapping of the charge carriers in deep energy levels of the silicon bulk and has been explained in detail in [27].

An obvious discrepancy in the measurements presented in Figure 20 is the very low relative signal amplitude of the sample F-42 ($9.7 \cdot 10^{14}$ $23\,GeV\,p/cm^2$). The weak, nearly shapeless signal is possibly the result of the optical properties of the diode that differ from the other samples. The refraction index of the surface at the opening for the laser might be different.

The weak signal could be caused by physical damage of the sample, as well. Namely, the soldering of the gold pin to the diode was observed to be damaged during the measurements. As the pin is the connector between the sample and the signal transmission line, it is plausible that the signal read out on the oscilloscope was influenced by the defect signal transmission.

It is possible to make some deductions from the measurement results of sample F-42, nonetheless. Figures 21 and 22 present the collected charge as a function of bias voltage for samples F-32 and F-42, respectively. The charge collection curve in Figure 21 is typical for FZ diodes that have undergone space charge sign inversion. The charge collection remains low at low bias voltages, as the maximum electric field has shifted to the back side of the diode while the red laser creates most carriers close to the front side. However, when the voltage reaches a sufficiently high value, the charge is collected from the back side, as well.

Figure 22, on the other hand, shows similar tendencies with regard to the shape of the charge collection graph. Thus, it seems that SCSI has occurred in sample F-42. However, the maximum bias voltage of 500 V may not be sufficient to enable charge collection from the back side.

In Figure 23, TCT signals from all sample types are compared that have been

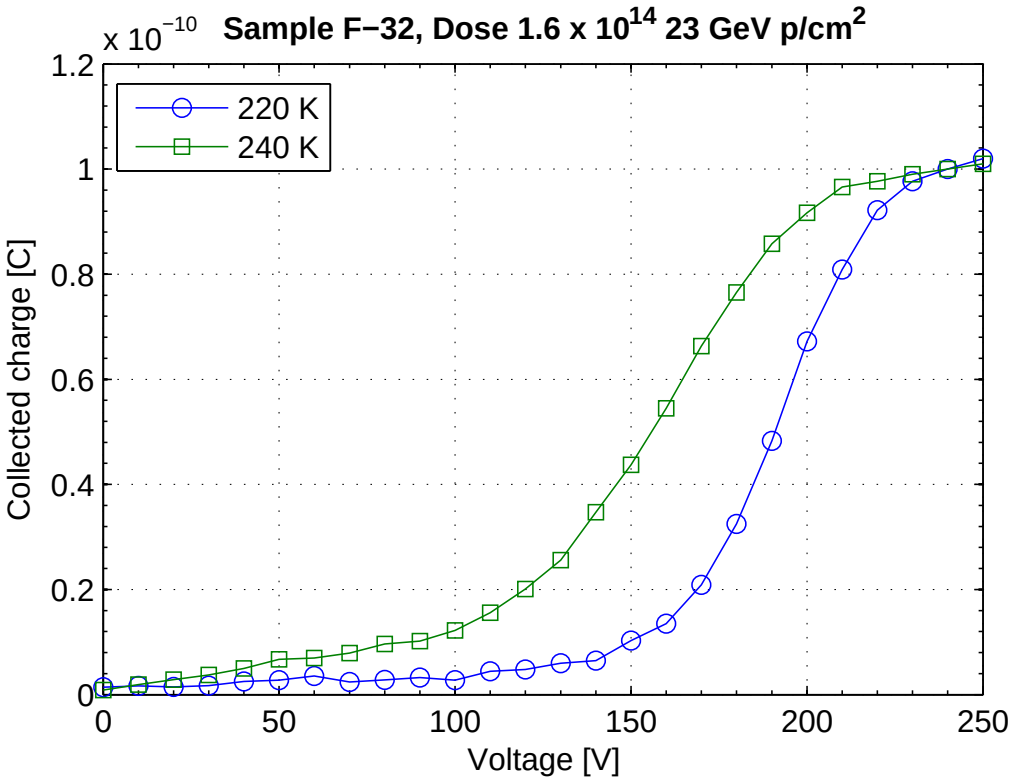

Figure 21: Charge collection in sample F-32 under red-laser illumination.

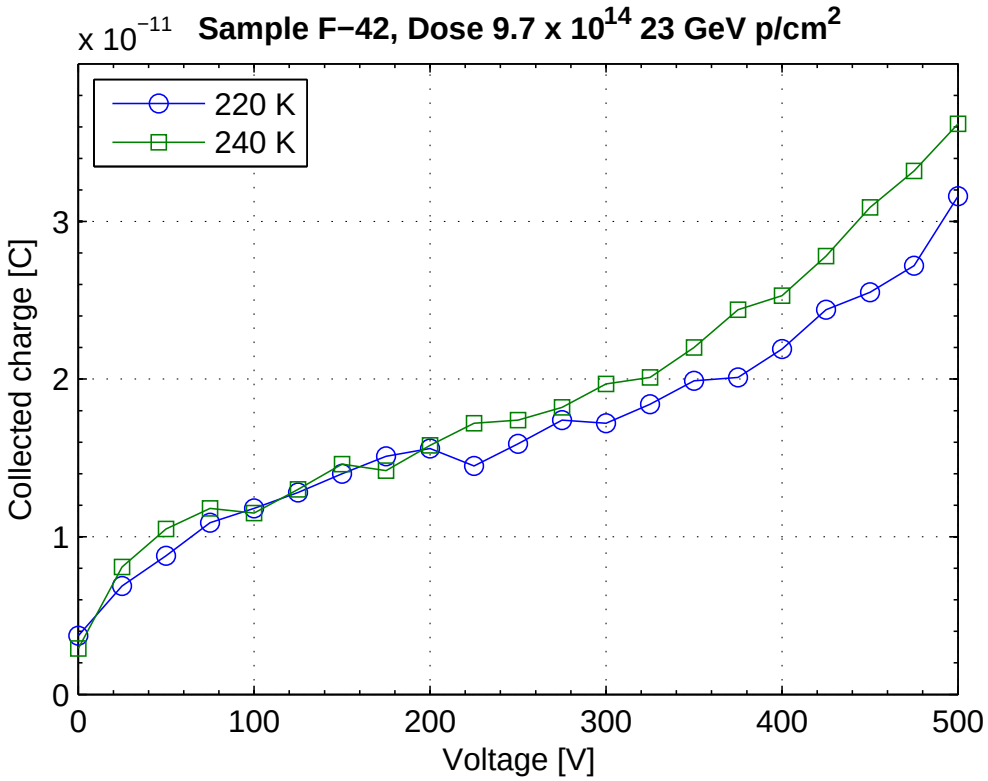

Figure 22: Charge collection in sample F-42 under red-laser illumination.

exposed to an irradiation dose of $1.3 \cdot 10^{15}$ $23\,GeV\,p/cm^2$. The amplitudes of the signals are scaled to a mutual, arbitrary maximum to simplify the comparison of the signal shapes. While both types of MCZ-Si diodes show very similar descending signal shapes at both temperatures, the shape of the n-type FZ diode is clearly ascending at 240 K, thus indicating SCSI. The signal shape of the FZ diode at 220 K delivers proof of double-peak formation in the electric field of the device.

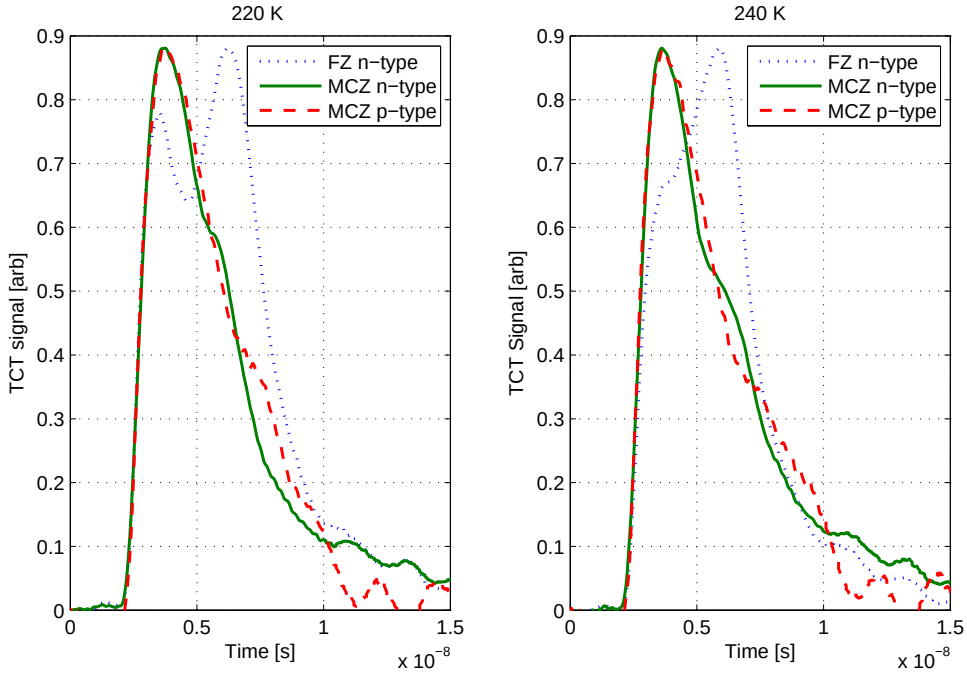

Figure 23: Comparison of diodes processed on different wafers. TCT signal values are scaled to a mutual maximum. Irradiation fluence on the samples: $1.3 \cdot 10^{15}$ $23\,GeV\,p/cm^2$.

The signal forms of the FZ diode can be explained by trapping in certain radiation induced defects. At 240 K, charge carriers get trapped and detrapped within the time corresponding to the laser trigger rate of the TCT setup. Thus, the defects contribute to the effective space charge, which leads to SCSI and one electric field maximum on the back side of the diode.

Lowering the temperature to 220 K raises the time the carriers stay captured to a higher value than that resulting from the laser trigger rate. Thus the defects do not contribute to the effective space charge any longer. The peak on the left rises

indicating another electric field maximum at the front side of the diode. In addition, it can be assumed that the aforementioned defects react with oxygen, as double-peak formation can be observed in neither type of MCZ diodes.

5.3 Annealing Experiment

The samples irradiated with a dose of $9.7 \cdot 10^{14}\,23\,GeV\,p/cm^2$, i.e., samples n-58, p-55, and F-70, were annealed at 80℃. The voltages of full depletion were determined at 240 K after each annealing step by the method explained in Section 4.1. The results for the depletion voltages in dependence of the cumulative annealing time are presented in Table 5 and Figure 24.

The shortest annealing time of 4 minutes caused the depletion voltage of the FZ diode to rise to 375 V. Further annealing raised the depletion voltages above 500 V, and thus they could not be determined exactly. Therefore, no V_{fd} values for that sample are illustrated in the figure. Furthermore, with no information about the depletion voltage, results for leakage currents or TCT measurements of fully depleted FZ diodes cannot be given.

Table 5: V_{fd} in [V] for each annealed sample after respective cumulative annealing time.

	4 min	12 min	28 min	60 min	124 min	252 min
n-58	252.3	215.7	205.0	221.1	274.2	349.9
p-55	-182.6	-183.2	-177.3	-224.0	-264.7	-320.7
F-70	374.9	>500	>500	>500	>500	>500

Both samples of MCZ-Si show characteristic behavior of beneficial annealing as the depletion voltages decrease with increasing annealing time until a minimum, which is followed by reverse annealing. The minimum depletion voltage appears for both diodes after the third annealing step, i.e., cumulative annealing of 28 minutes at 80℃. This corresponds roughly to one month in room temperature.

As can be seen in Figure 24, the absolute values of the depletion voltages are generally slightly lower for the p-type than for the n-type samples. For example, the minimum value of V_{fd} for sample p-55 equals –177 V, whereas the corresponding

value for n-58 is 205 V. The absolute value of V_{fd} has thus decreased by about 20 V from the value before annealing in sample p-55. The decrease is about 50 V for sample n-58. The property of beneficial annealing is characteristic for n-type detectors that have undergone SCSI and p-type detectors, as has been explained in Section 3.3.

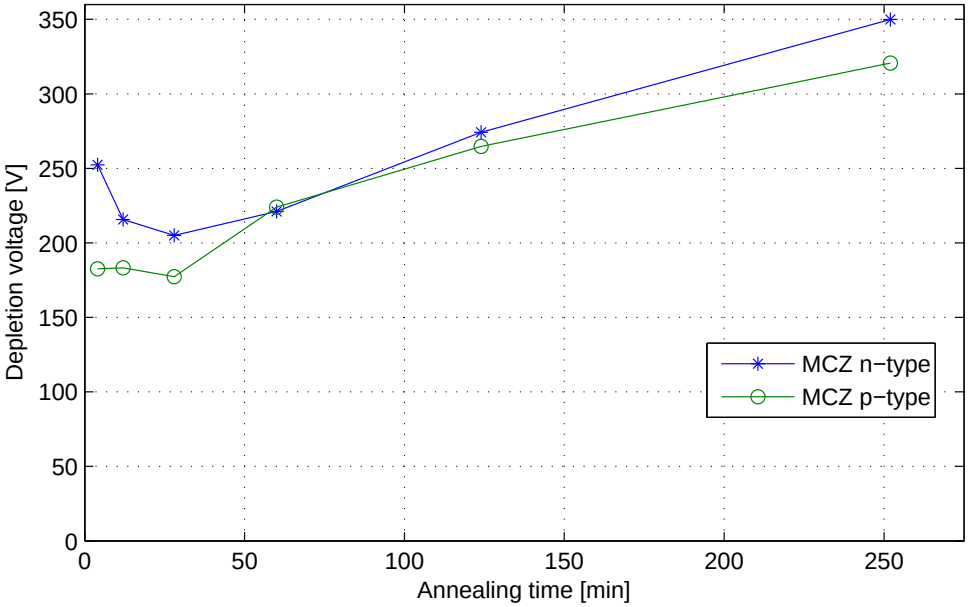

Figure 24: Absolute values of depletion voltages after annealing.

Figures 25 and 26 show the leakage currents I_{leak} in the annealed diodes biased with a voltage equaling V_{fd} at the two measurement temperatures 240 K and 220 K. As can be seen from the figures, the shape of the graphs depicting the evolution of I_{leak} values with cumulative annealing time stay similar in the two temperatures with $\Delta T = 20K$, although the values differ by one order of magnitude. As the current is strongly temperature dependent, the leakage current results in different temperatures should not be compared otherwise without scaling them to a reference temperature.

For both types of detectors, the leakage current decreases during beneficial annealing and even until after the fourth annealing step. The leakage current in the p-type sample steadies at both temperatures as expected with regard to previous results.

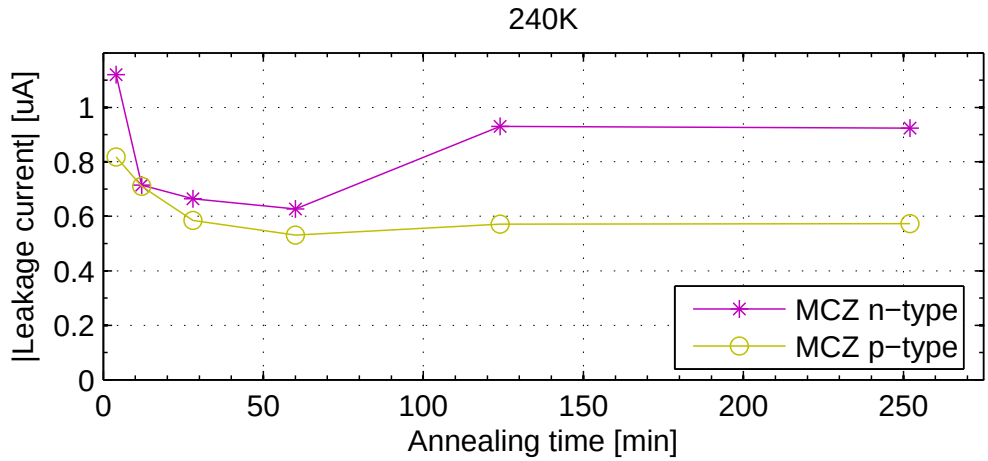

Figure 25: Absolute values of leakage currents after annealing measured at 240 K.

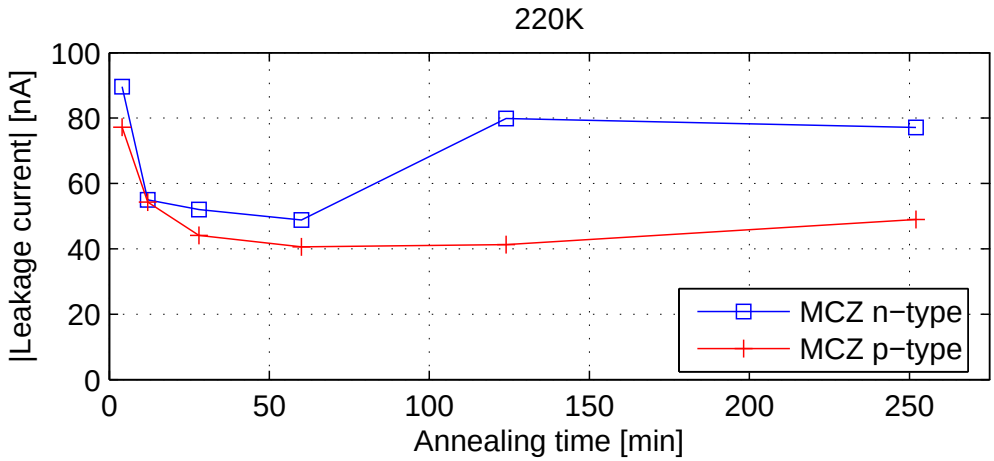

Figure 26: Absolute values of leakage currents after annealing measured at 220 K.

However, the I_{leak}-values at both temperatures start increasing again during the last two annealing steps.

The depletion voltages for the long-term annealed samples were in general harder to determine with the used graphical method, as the saturation of the collected charge shifted close to the maximum bias voltage of 500 V. Naturally, this leads to inaccuracies in the determination of leakage currents, as well. Furthermore, the laser operation was not stable during the characterization measurements of the n-type diode after the second to last annealing step. These factors might have had an impact on the results, as well.

The response of the MCZ diodes is better at the lower temperature of 220 K throughout this study. Therefore, TCT signals measured at this temperature are presented in Figures 27 and 28 to make the influence of annealing on the properties of the n-type and p-type samples more perceptual.

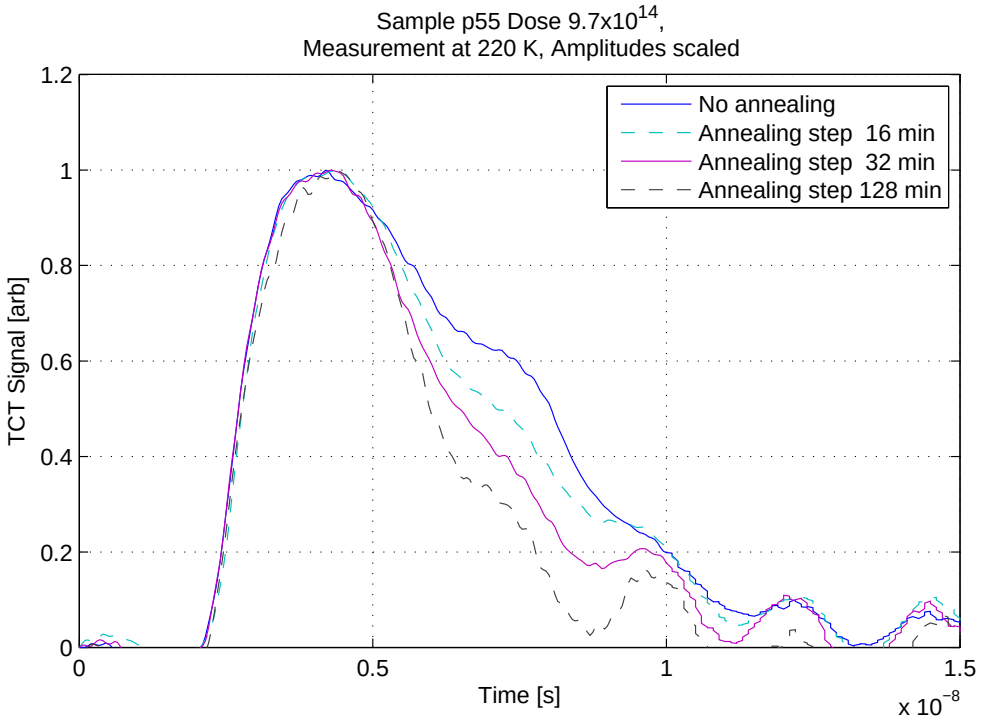

Figure 27: Fully depleted ($V \approx V_{fd} + 100V$), annealed MCZ p-type diode measured at 220 K.

As the differences in signal intensity were small in the p-type detector, save the

measurement after the last annealing step, the chosen amplitudes for Figure 27 are scaled to 1 with the purpose of easier comparison. It is evident from the figure that the signal shape changes mostly by narrowing after annealing, while the general form shows no great changes. Annealing narrows the signal in a similar manner as high irradiation fluence, as the charge collection efficiency degrades because of trapping.

Sample n-58, on the other hand, is affected differently by annealing. While the signal width remains approximately constant until the second to last annealing step, the signal shape changes clearly from descending to ascending between the third and fourth steps. The ascending signal shape is clear evidence for SCSI. This conclusion holds, even if the SCSI has started earlier, as discussed before. In such a case, the inversion to an ascending signal can be interpreted as sufficient excess of acceptor type doping to make the shifted junction asymmetrical enough to be visible in the TCT measurement despite of trapping. After the last annealing step and total annealing time of 252 minutes, the signal becomes more narrow, as well, because trapping hinders reading out the full generated signal.

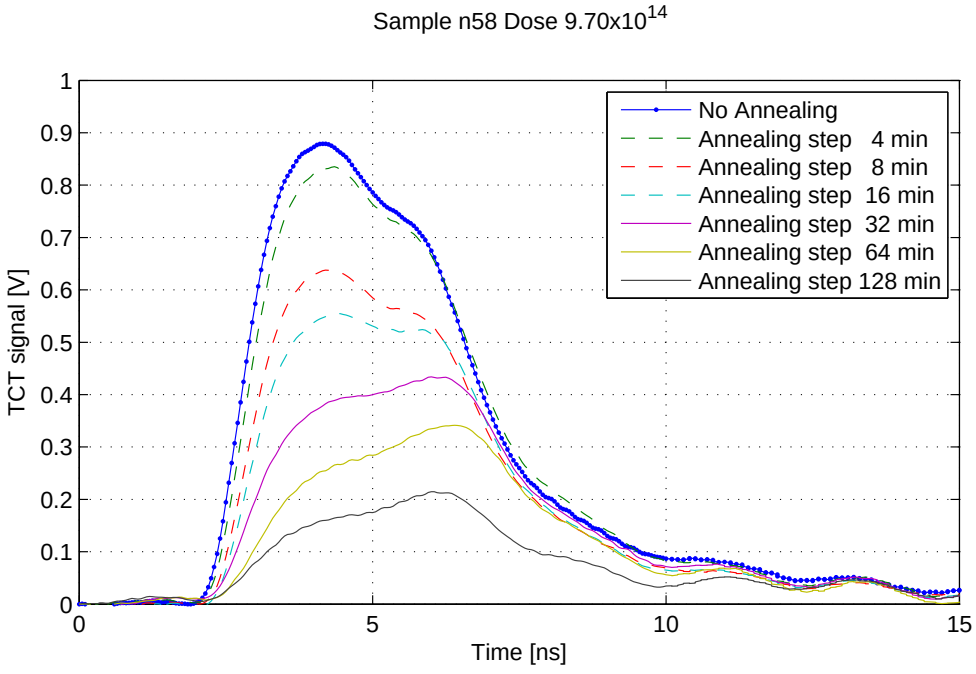

Figure 28: Fully depleted ($V \approx V_{fd} + 100V$), annealed MCZ n-type diode measured at 220 K.

6 Summary

This thesis investigated properties of silicon particle detectors by means of the transient current technique. The TCT measurements were conducted on different types of sample diodes. Diodes were compared that had been processed on wafers fabricated by the magnetic Czochralski method and by the float zone method. Differences between n-type and p-type MCZ diodes were examined, as well.

The sample diodes were characterized via parameters obtained from the measurements: voltage of full depletion, leakage current, and charge collection. The distribution of the electric field in the diode structures was examined qualitatively, as well. Additionally, the annealing behavior of different detector types was investigated after heat treatment at 80℃.

It was found, that MCZ-Si diodes withstand both irradiation as well as annealing better than FZ-Si diodes when judged by parameters, such as depletion voltage or leakage current. Comparison of collected data from n-type and p-type MCZ-Si diodes succeeded, as well. The results were supporting the presumption that it may be possible to use n^+-p-p^+ structures for future particle detector applications in high energy physics experiments.

In this study, the p-type samples seemed less sensitive than the n-type samples to both irradiation as well as annealing, thus indicating advanced radiation hard properties. It is also possible to make one-sided detector structures of p-type bulk, as the read-out electronics are preferably connected to the n-type implantation on the front side of the detectors. The material properties found in this thesis as well as practical electronic aspects make p-type MCZ-Si attractive for detector applications in HEP experiments.

Not only the current silicon detectors in the LHC experiments are to be replaced in the coming years. The next level, the Super-LHC (S-LHC) with even higher collision rates, has already been planned to start in 10 to 15 years. The decisions have not yet been made concerning the tracker detectors and their final realization in the S-LHC.

Therefore, various studies are being carried out to enhance radiation hardness and suitability of silicon particle detectors for particle accelerator experiments.

For example, overcoming the problem of trapping, that reduces CCE, has been investigated within the CERN RD39 Collaboration. As the depletion voltages of the detectors reach values close or over the operational limits of the experiments, the charge collection efficiency becomes more important. One possible solution could be current injected detectors (CID) operated at a temperature of approximately 220 K. These are practically forward-biased regular detectors taking advantage of the strong temperature dependence of the detrapping coefficient. As can be seen, the work to improve radiation hardness of the silicon particle detectors remains continuously relevant.

References

[1] CERN. LHC: Facts and figures. http://public.web.cern.ch/public/en/LHC/Facts-en.html. Referred 2.12.2008.

[2] CERN. Missing Higgs. http://public.web.cern.ch/public/en/Science/Higgs-en.html. Referred 2.12.2008.

[3] CERN. CMS – Physics – Hunting the Higgs boson. http://cms-project-cmsinfo.web.cern.ch/cms-project-cmsinfo/Physics/HuntingHiggs/CMS.html. Referred 2.12.2008.

[4] Michel Della Negra, L. Foa, A. Herve, and Achille Petrilli. *CMS physics: Technical Design Report*. Technical Design Report CMS. CERN, Geneva, 2006.

[5] Communication Group. *CERN LHC: the guide. faq. frequently asked questions.* CERN-Brochure-2008-001-Eng. CERN, Geneva, Jan 2008.

[6] CERN. How the LHC works. http://cms-project-cmsinfo.web.cern.ch/cms-project-cmsinfo/Physics/HuntingHiggs/CMS.html. Referred 9.12.2008.

[7] CERN. CMS – Physics. http://cms-project-cmsinfo.web.cern.ch/cms-project-cmsinfo/Physics/index.html. Referred 9.12.2008.

[8] CERN. CMS detector overview. http://cms-project-cmsinfo.web.cern.ch/cms-project-cmsinfo/Detector/FullDetector/index.html. Referred 9.12.2008.

[9] *The CMS tracker: addendum to the Technical Design Report*. Technical Design Report CMS. CERN, Geneva, 2000.

[10] Z. Li et al. Investigation of the oxygen-vacancy (A-center) defect complex profile in neutron irradiated high resistivity silicon junction particle detectors. *IEEE Transactions on Nuclear Science*, 39(6):1730–1738, Dec 1992.

[11] G Lindstrom, S Watts, and F Lemeilleur. 3rd rd48 status report: the rose collaboration (research and development on silicon for future experiments). Technical Report CERN-LHCC-2000-009, CERN, Geneva, Dec 1999.

[12] V. Eremin, N. Strokan, E. Verbitskaya, and Z. Li. Development of transient current and charge techniques for the measurement of effective net concentration of ionized charges (N_{eff}) in the space charge region of p-n junction detectors. *Nucl. Instrum. Meth.*, A372:388–398, 1996.

[13] S. M. Sze. *Physics of semiconductor devices, 2nd edition.* New York, Wiley-Interscience, 1981.

[14] C. Amsler et al. Review of particle physics. *Phys. Lett.*, B667:1, 2008.

[15] A. Vasilescu and G. Lindstrom. Notes on the fluence normalisation based on the NIEL scaling hypothesis. Technical Report ROSE/TN/2000-02, CERN, Geneva, 2000.

[16] G. Lindstrom. Radiation damage in silicon detectors. *Nucl. Instrum. Methods Phys. Res., A*, 512(DESY-2002-199-A):30–43, Nov 2002.

[17] M. Huhtinen. Simulation of non-ionising energy loss and defect formation in silicon. *Nucl. Instrum. Methods Phys. Res., A*, 491(1-2):194–215, 2002.

[18] M. Moll. *Radiation damage in silicon particle detectors: microscopic defects and macroscopic properties*. PhD thesis, Hamburg Univ., Hamburg, 1999.

[19] M. Moll and M. Bruzzi. RD50 Status Report 2007 – Radiation hard semiconductor devices for very high luminosity colliders. Technical Report LHCC-RD-015. CERN-LHCC-2008-001, CERN, Geneva, Jan 2008.

[20] J. Harkonen et al. RD39 Status Report 2007. Technical Report LHCC-RD-014. CERN-LHCC-2007-028, CERN, Geneva, Nov 2007.

[21] V. Eremin, Z. Li, and I. Ilyashenko. Trapping induced N_{eff} and electrical field transformation at different temperatures in neutron irradiated high resistivity silicon detectors. *Nucl. Instrum. Meth.*, A360:458–462, 1995.

[22] F. Lemeilleur, G. Lindstrom, and S. Watts. 2nd ROSE/RD48 Status Report. 1998.

[23] E. Tuominen et al. Radiation hardness of Czochralski silicon studied by 10-MeV and 20-MeV protons. *Nuclear Science, IEEE Transactions on*, 50(6):1942–1946, Dec. 2003.

[24] J. Harkonen, E. Tuovinen, P. Luukka, H. K. Nordlund, and E. Tuominen. Magnetic Czochralski silicon as detector material. *Nucl. Instrum. Meth.*, A579:648–652, 2007.

[25] J. Harkonen et al. Low-temperature TCT characterization of heavily proton irradiated p-type magnetic Czochralski silicon detectors. *Nucl. Instrum. Meth.*, A583:71–76, 2007.

[26] G. Casse. Development of p-type detectors for present LHC and luminosity upgrades. *Nuclear Instruments and Methods in Physics Research Section A: Accelerators, Spectrometers, Detectors and Associated Equipment*, 579(2):623 – 627, 2007. Proceedings of the 6th "Hiroshima" Symposium on the Development and Application of Semiconductor Detectors.

[27] V. Eremin, E. Verbitskaya, and Z. Li. The origin of double peak electric field distribution in heavily irradiated silicon detectors. *Nucl. Instrum. Meth.*, A476:556–564, 2002.

[28] G. Kramberger and D. Contarato. How to achieve highest charge collection efficiency in heavily irradiated position-sensitive silicon detector. *Nucl. Instrum. Meth.*, A560:98–102, 2006.

[29] M. Moll, E. Fretwurst, and G. Lindstrom. Leakage current of hadron irradiated silicon detectors - material dependence. *Nucl. Instrum. Meth.*, A426:87–93, 1999.

[30] G. Lindstrom et al. Radiation hard silicon detectors – developments by the RD48 (ROSE) Collaboration. *Nucl. Instrum. Meth.*, A466:308–326, 2001.

[31] G. Kramberger, V. Cindro, I. Mandic, M. Mikuz, and M. Zavrtanik. Determination of effective trapping times for electrons and holes in irradiated silicon. *Nucl. Instrum. Meth.*, A476:645–651, 2002.

[32] S. Ramo. Currents induced by electron motion. *Proc. IRE*, 27:584–585, 1939.

[33] J. Harkonen et al. The Cryogenic Transient Current Technique (C-TCT) measurement setup of CERN RD39 Collaboration. *Nucl. Instrum. Meth.*, A581:347–350, 2007.